NeuroImage 253 (2022) 119092

Contents lists available at ScienceDirect

NeuroImage

journal homepage: www.elsevier.com/locate/neuroimage

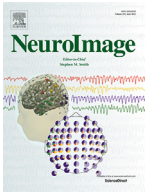

Multi-parameter quantitative mapping of R1, R2*, PD, and MTsat is reproducible when accelerated with Compressed SENSE

Ronja C. Berg[a,b,*], Tobias Leutritz[c], Nikolaus Weiskopf[c,d], Christine Preibisch[a,b,e]

[a] Technical University of Munich, School of Medicine, Klinikum rechts der Isar, Department of Diagnostic and Interventional Neuroradiology, Munich, Germany
[b] Technical University of Munich, School of Medicine, Klinikum rechts der Isar, Department of Neurology, Munich, Germany
[c] Max Planck Institute for Human Cognitive and Brain Sciences, Department of Neurophysics, Leipzig, Germany
[d] Felix Bloch Institute for Solid State Physics, Faculty of Physics and Earth Sciences, Leipzig University, Leipzig, Germany
[e] Technical University of Munich, School of Medicine, Klinikum rechts der Isar, TUM Neuroimaging Center, Munich, Germany

ARTICLE INFO

Keywords:
Multi-parameter mapping
Quantitative MRI
Compressed SENSE
Imaging acceleration
Reproducibility

ABSTRACT

Multi-parameter mapping (MPM) magnetic resonance imaging (MRI) provides quantitative estimates of the longitudinal and effective transverse relaxation rates R1 and R2*, proton density (PD), and magnetization transfer saturation (MTsat). Thereby, MPM enables better comparability across sites and time than conventional weighted MRI. However, for MPM, several contrasts must be acquired, resulting in prolonged measurement durations and thus preventing MPM's application in clinical routines. State-of-the-art imaging acceleration techniques such as Compressed SENSE (CS), a combination of compressed sensing and sensitivity encoding, can be used to reduce the scan time of MPM. However, the accuracy and precision of the resulting quantitative parameter maps have not been systematically evaluated. In this study, we therefore investigated the effect of CS acceleration on the fidelity and reproducibility of MPM acquisitions.

In five healthy volunteers and in a phantom, we compared MPM metrics acquired without imaging acceleration, with the standard acceleration (SENSE factor 2.5), and with Compressed SENSE with acceleration factors 4 and 6 using a 32-channel head coil. We evaluated the reproducibility and repeatability of accelerated MPM using data from three scan sessions in gray and white matter volumes-of-interest (VOIs).

Accelerated MPM provided precise and accurate quantitative parameter maps. For most parameters, the results of the CS-accelerated protocols correlated more strongly with the non-accelerated protocol than the standard SENSE-accelerated protocols. Furthermore, for most VOIs and contrasts, coefficients of variation were lower when calculated from data acquired with different imaging accelerations within a single scan session than from data acquired in different scan sessions with the same acceleration method.

These results suggest that MPM with Compressed SENSE acceleration factors up to at least 6 yields reproducible quantitative parameter maps that are highly comparable to those acquired without imaging acceleration. Compressed SENSE can thus be used to considerably reduce the scan duration of R1, R2*, PD, and MTsat mapping, and is highly promising for clinical applications of MPM.

1. Introduction

Magnetic resonance imaging (MRI) is one of the most widespread and powerful techniques for diagnostic imaging. Its unparalleled and highly versatile soft tissue contrast is predominantly influenced by the interplay of tissue proton density and relaxation parameters (Weiskopf et al., 2021). While everyday clinical routines still mostly rely on qualitative MRI using weighted images across a wide variety of contrasts, quantitative MRI (qMRI) promises better comparability across sites and time as well as detectability of systemic tissue changes beyond

Abbreviations: ACR, anterior corona radiata; AFI, actual flip angle imaging; ANOVA, analysis of variance; CoV, coefficient of variation; CS, Compressed SENSE; GM, gray matter; ISC, imperfect spoiling correction; MPM, multi-parameter mapping; MR, magnetic resonance; MRI, magnetic resonance imaging; MT, magnetization transfer; MTw, MT-weighted; MTsat, magnetization transfer saturation; p.u., percent units; PD, proton density; PDw, PD-weighted; qMRI, quantitative MRI; R1, longitudinal relaxation rate; R2*, effective transverse relaxation rate; RF, radiofrequency; SENSE, sensitivity encoding; SNR, signal-to-noise ratios; SPM, Statistical Parametric Mapping; T_1, longitudinal relaxation time; T1w, T_1-weighted; T_2, transverse relaxation time; T_2^*, effective transverse relaxation time; TR, repetition time; VFA, variable flip angle; VOI, volume-of-interest; WM, white matter.

* Corresponding author at: Technical University of Munich, School of Medicine, Klinikum rechts der Isar, Department of Diagnostic and Interventional Neuroradiology, Ismaninger Str. 22, 81675 München, Germany.

E-mail addresses: ronja.berg@tum.de (R.C. Berg), tleutritz@cbs.mpg.de (T. Leutritz), weiskopf@cbs.mpg.de (N. Weiskopf), preibisch@tum.de (C. Preibisch).

https://doi.org/10.1016/j.neuroimage.2022.119092.
Received 12 October 2021; Received in revised form 7 March 2022; Accepted 8 March 2022
Available online 11 March 2022.

circumscribed lesions, edemas, and necroses (Weiskopf et al., 2021). While a wide variety of parameters can be quantified by means of MRI, the most basic ones, i.e., proton density (PD), (effective) transverse relaxation time $T_2(^*)$, and longitudinal relaxation time T_1, are most often referred to when talking about quantitative MRI. These parameters allow calculation of synthetic magnetic resonance (MR) images with any commonly used or physically impossible contrast (Callaghan et al., 2016; Wehrli et al., 1984), or may serve as a basis for deriving more specific physiological parameters via biophysical modeling, which has been referred to as in-vivo histology (Weiskopf et al., 2021). However, in numerous studies, quantitative T_1, $T_2(^*)$, and PD parameter values have already shown benefits on their own as potential biomarkers in a wide range of neurological diseases, e.g., multiple sclerosis (Reitz et al., 2017), cerebral small vessel disease (Brandhofe et al., 2020), or tumors (Lescher et al., 2015) (see (Seiler et al., 2021) for a recent review).

Although quantitative MRI techniques have been applied in clinical studies since the mid-eighties of the 20th century (Bottomley et al., 1987; Holland et al., 1986; Just and Thelen, 1988), qMRI has not yet reached clinics. A major reason is that qMRI requires acquisitions of several different contrasts and complex evaluation routines (Tofts, 2003). Since patients are often less compliant than healthy volunteers, high speed acquisitions are highly beneficial for clinical applications. Fortunately, in recent years, quantitative MRI techniques have increasingly been accelerated and refined (Cooper et al., 2020; Fujita et al., 2021; Leutritz et al., 2020), which raises hopes that qMRI may finally find its way into the clinical routine.

One currently well-established approach is multi-parameter mapping (MPM) of T_1, $T_2{}^*$, PD, and magnetization transfer (MT) saturation (MTsat) (Helms et al., 2008; Weiskopf et al., 2013) using a modified variable flip angle radiofrequency (RF) spoiled multi-echo gradient-echo acquisition and modeling. This approach is implemented in a software toolbox for in-vivo histology using MRI (Tabelow et al., 2019; Weiskopf et al., 2015). It has already been widely applied to investigate microstructural properties of neural tissue (Callaghan et al., 2014; Freund et al., 2011; Grabher et al., 2015; Seif et al., 2018; Weiskopf et al., 2013; Ziegler et al., 2018) and validated in multi-center reproducibility studies (Leutritz et al., 2020; Weiskopf et al., 2013). While a measurement duration of about 20 minutes is acceptable for many clinical studies, this must be further reduced to be applicable in routine clinical protocols.

Over the last decades, the scan duration of MRI acquisitions has constantly been reduced not only due to faster gradient switching, but mainly due to multi-channel receive coils and evermore sophisticated undersampling and reconstruction techniques such as parallel imaging. One technique that combines parallel imaging, more specifically sensitivity encoding (SENSE) (Pruessmann et al., 1999) and compressed sensing (Candès et al., 2006a, b; Donoho, 2006; Lustig et al., 2008) is commercially available as Compressed SENSE (Geerts-Ossevoort et al., 2018) on Philips scanners. It has facilitated considerably reduced acquisition durations in weighted 3D clinical MRI without compromising diagnostic quality (Ding et al., 2021; Duan et al., 2020; Eichinger et al., 2019; Nam et al., 2019; Vranic et al., 2019). Furthermore, CS and similar techniques have proven valuable acceleration methods to shorten scan times for several quantitative MRI techniques (Boyarko et al., 2021; Jaeger et al., 2020; Kaga et al., 2021; Kocaoglu et al., 2021; Mussard et al., 2020). Recently, Compressed SENSE has also been used to speed up 3D acquisitions for combined mapping of several quantitative measures in a phantom (Murata et al., 2021), and we obtained preliminary evidence that this also holds *in vivo* (Berg et al., 2020), which would facilitate the use of quantitative biomarkers in clinical routines.

The aim of this study was, therefore, to investigate the effect of Compressed SENSE acceleration on the fidelity and reproducibility of quantitative multi-parameter mapping of the longitudinal and effective transverse relaxation rates R1 (= $1/T_1$) and R2* (= $1/T_2{}^*$), PD, and MTsat. To this end, we compared scans with standard acceleration (SENSE factor 2.5) and Compressed SENSE acceleration factors 4 and 6 to a fully sampled non-accelerated scan. In addition, we investigated repeatability across three scan sessions in five healthy volunteers.

2. Methods

2.1. Participants and phantom

This study was approved by the local medical ethical committee at the Klinikum rechts der Isar, Technical University of Munich (TUM). After providing informed written consent for participation in this study, five healthy volunteers (three females, age range: 23-49 years, average age: 30.4 years in the first scan) underwent MRI at the Department of Neuroradiology, Klinikum rechts der Isar, TUM.

All five participants were scanned four times over a period of approximately 14 months. In three scan sessions (Scans A-C), the MPM protocol was run three times each, including all three accelerated protocols in each scan session. In an additional scan session, all sequences were scanned without any imaging acceleration ("No-Acc" scan). Scan A was performed about ten months prior to Scan B. Scan C was performed about four months after Scan B. The non-accelerated scan was performed around the same time as Scan B but in a separate session.

Additionally, the NIST/ISMRM system phantom (System Standard Model 130, CaliberMRI (previously QalibreMD), Boulder, Colorado; https://www.nist.gov/programs-projects/quantitative-mri) was scanned in three separate scan sessions at room temperature (about 20°C). For the phantom scans, the three accelerated protocols and the non-accelerated protocol were combined and performed jointly in each scan session. This phantom contains components of known reference T_1 and PD values.

2.2. Data acquisition

Data acquisition was performed on a Philips Ingenia Elition X 3 T MR system (Philips Healthcare, R5.5.2 (Scan A) or R5.6.1.0 (Scan B, C, and "No-Acc" scan), Best, NL) using a 32-channel RF receive head coil. In scan sessions A-C, the entire protocol was scanned with three different imaging accelerations but with otherwise identical imaging parameters. Aside from the standard SENSE technique for the lowest acceleration factor, we chose Compressed SENESE as the acceleration method for higher reduction factors since it was found to be less prone to artifacts and to provide better SNR (Akçakaya et al., 2014; Cho et al., 2019; Eichinger et al., 2019; Geerts-Ossevoort et al., 2018). The applied accelerations comprised the standard acceleration using sensitivity encoding (Pruessmann et al., 1999) with acceleration factors AP: 2 and RL: 1.25 (scan duration of 20 minutes) and Compressed SENSE (Geerts-Ossevoort et al., 2018) with acceleration factors of CS = 4 (15:40 minutes) and CS = 6 (10:30 minutes) for a 1mm^3 isotropic voxel size. Here, the acceleration factors describe the reduction of k-space samples acquired with the respective acceleration method. The acquisition duration, however, is not necessarily linearly related to the reduction of k-space lines, but is additionally influenced by other factors such as non-accelerated preparatory scans. For the same spatial resolution, the "No-Acc" protocol without any imaging acceleration had a scan duration of 45:30 minutes (see Fig. 1A).

All imaging sequences were based on a 3D RF-spoiled multi-echo gradient-echo sequence (fast field echo) with six echoes (first echo time and echo spacing TE1/ΔTE = 2.4/2.4 ms). The sequences used a phase increment of 150°, bipolar readout gradients (no flyback), and no flow compensation. They had a $1 \times 1 \times 1$ mm^3 resolution, a water-fat shift of 0.9 pixel, and used a partial Fourier factor of ~0.6 ("half scan" Y-factor). The protocol comprised three main sequences: a T_1-weighted sequence (T1w) with repetition time TR = 18 ms, flip angle $\alpha = 25°$, and RF excitation pulse duration t_{ex} = 0.954 ms; a PD-weighted sequence (PDw) with TR = 18 ms, $\alpha = 4°$, and t_{ex} = 0.669 ms; and an MT-weighted sequence (MTw) with TR = 48 ms, $\alpha = 6°$, t_{ex} = 0.669 ms, MT saturation

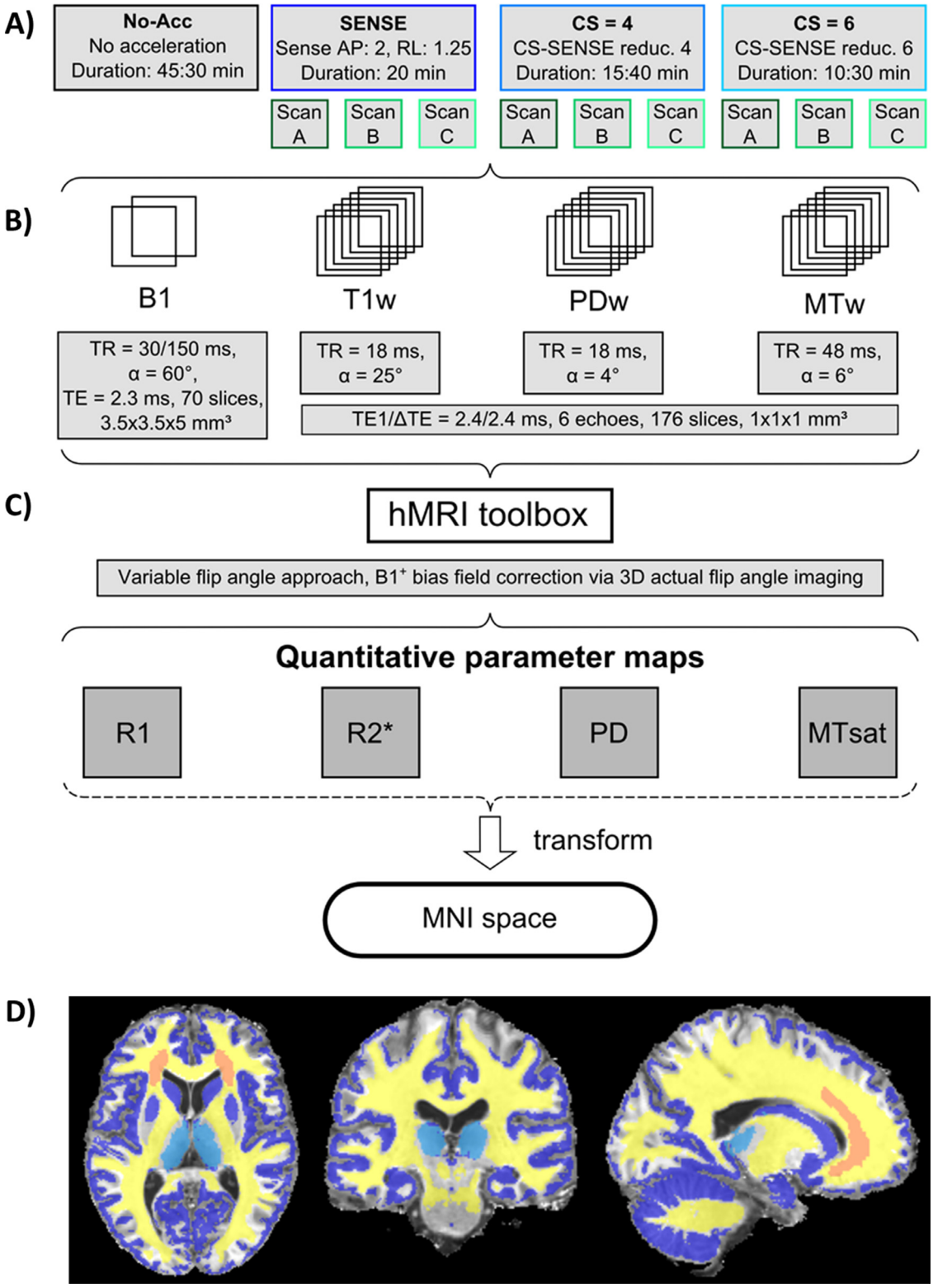

Fig. 1. Methodological overview including: A) protocol variants using different imaging accelerations, B) acquisition parameters, C) processing details, and D) utilized gray and white matter volumes-of-interest (VOIs). The protocols accelerated with SENSE = 2.5, CS = 4, and CS = 6 were each scanned three times (Scans A-C). The VOIs used for the analysis of quantitative parameter values were common whole-brain gray matter (blue), whole-brain white matter (yellow), common voxels within the thalamus (azure), and common voxels within the anterior corona radiata (orange).

flip angle $\alpha_{MT} = 220^{\circ}$, MT pulse duration $t_{MT} = 8$ ms, and MT saturation off-resonance frequency $f_{MT} = 1{,}000$ Hz. Both RF excitation pulses and MT pulses had a sinc-gauss-shape. The images were acquired in sagittal orientation with frequency encoding (readout) in the foot-head direction, an anterior-posterior (AP) primary phase encoding (PE_1) direction (fold-over), a right-left (RL) secondary phase encoding (PE_2) direction, and a field-of-view of 240 × 240 × 176 mm^3 (read x PE_1 x PE_2). For a voxel-wise $B1^+$ bias field correction using the 3D actual flip angle imaging (AFI) method (Yarnykh, 2007), B1 mapping was performed with a voxel size of 3.5 × 3.5 × 5 mm^3 and a field-of-view of 240 × 240 × 175 mm^3. The order of sequences within each MPM protocol was the same for all scans (1. B1 map, 2. T1w, 3. PDw, 4. MTw), but the order of accelerated protocols within the scan sessions A-C was permuted across participants and scan sessions. A summary of the imaging parameters is shown in the methodological overview in Fig. 1B.

2.3. Parameter map calculation

Unless stated otherwise, all data processing and analyses were performed using MATLAB (R2020a, The Mathworks, Natick, MA, United States; RRID: SCR_001622). DICOM to NIfTI conversion was performed using the hMRI toolbox (version v0.1.3-dev; RRID: SCR_017682; https://github.com/tleutritz-cbs/hMRI-toolbox) and the Statistical Parametric Mapping (SPM) framework (SPM12, version v7771; RRID: SCR_007037; https://www.fil.ion.ucl.ac.uk/spm/software/spm12/). All *in vivo* images were then reoriented via rigid-body transformation using the "Auto-reorient" function provided by the hMRI toolbox to correct for angulations of the head and to place the origin at the anterior commissure. Quantitative parameter maps of relaxation rates R1 and R2*, proton density, and magnetization transfer saturation (Fig. 1C) were calculated via the variable flip angle (VFA) approach (Baudrexel et al., 2018; Preibisch and Deichmann, 2009) in combination with multiple gradient echoes using SPM and the hMRI toolbox (Tabelow et al., 2019). Information from all three multi-echo contrasts was combined for estimation of R2* (Weiskopf et al., 2014). Default configuration parameters were used except for a threshold of 10^8 for the PD map before bias field correction (which is scanner dependent) and a threshold of 15 percent units (p.u.) for the MTsat values (which depends on the utilized MT parameters).

Residual bias in the apparent R1 maps due to insufficient RF spoiling (Preibisch and Deichmann, 2009) was accounted for using imperfect spoiling correction (ISC) (Baudrexel et al., 2018) customized to the sequence specific phase increment.

2.4. Additional processing of phantom data

Since the standard procedures in the hMRI toolbox are optimized for human brain imaging, a few additional processing steps had to be performed for processing the phantom data. First, the phantom data were masked manually using ITK-SNAP (RRID: SCR_002010; http://www.itksnap.org) to obtain a mask of the whole volume of the phantom, which was needed for parameter map calculation. Furthermore, the RF transmit bias field was calculated based on the masked PD data set. Finally, the PD map was calibrated to a volume-of-interest (VOI) of known PD value segmented from the uncorrected PD data set (otherwise, the default calibration is based on the segmentation of whole-brain white matter (WM) and a standard WM PD value, which is not applicable to phantom data).

2.5. Segmentation and normalization to MNI space of in vivo data

All ten data sets per participant were acquired with a similar head orientation and alignment. The nine accelerated data sets per participant were first registered to the single non-accelerated data set using SPM's "co-register" module and trilinear interpolation (with 7 × 7 Gaussian Histogram smoothing, 4 × 2 separation distance between sampled points, no wrapping, no masking). Subsequently, registered and head-masked R1 parameter maps were segmented into tissue probability maps using SPM's unified segmentation (Ashburner and Friston, 2005) via the "segmentation" module implemented in the hMRI toolbox. The set of all fifty gray matter (GM) segmentations and the set of all fifty WM segmentations (from the five participants and their ten scans each) were warped together using the "Run Dartel" module of the hMRI toolbox with default parameters. Thereby, the tissue class images were iteratively aligned to their own average and a study specific template was created from their average. The final template and the individual deformation fields were then used to align the images with MNI space by affine transformation via the "Normalise to MNI Space" module with a voxel size of 1 × 1 × 1 mm^3, a suitable bounding box, and otherwise default parameters.

2.6. Volume-of-interest definition in vivo data

From the MNI normalized data, four volumes-of-interest were derived for further analyses (see Fig. 1D). Common whole-brain segments of GM and WM were calculated as the intersection of all fifty R1-based segmentations with individual tissue probability > 0.5 for either GM or WM (five participants, ten scans per participant). In addition to these whole-brain GM and WM VOIs, two smaller, anatomically defined regions were selected from atlases (https://fsl.fmrib.ox.ac.uk/fsl/fslwiki/Atlases) included in the FSL framework (Smith et al., 2004). The GM thalamus region was defined according to FSL's "Oxford Thalamic Connectivity Probability Atlas" (Behrens et al., 2003) including only voxels that were contained in all individual GM segmentations across all scans of all volunteers. This was calculated by intersecting all segments of the thalamus region from the atlas with the common whole-brain GM segment. The anterior corona radiata (ACR) region within WM consisted of the voxels defined as anterior corona radiata right and left in FSL's ICBM-DTI-81 white-matter labels atlas (Mori et al., 2005) that were likewise contained in all individual segmentations. This was calculated by intersecting the ACR region from the atlas with the common whole-brain WM segment.

Additionally, a global outlier mask was calculated containing voxels with non-physiologic parameter values. This was calculated as an intersection of all voxels with negative values in any of the imaging contrasts (for any of the accelerations or scans and any of the participants) and voxels with $R2^* > 40\ s^{-1}$ (i.e., $T_2^* < 25$ ms). These voxels were excluded from the four defined VOIs for further analysis. The final whole-brain GM VOI contained ~443,000 voxels, the whole-brain WM VOI ~390,000 voxels, the thalamus (GM) ~10,000 voxels, and the ACR (WM) ~13,000 voxels.

2.7. Volume-of-interest definition in phantom data

The NIST/ISMRM system phantom contains fiducial spheres with defined T_1, T_2, or PD values. From the spheres with defined T_1 values, the four spheres with the highest T_1 values were most comparable to physiological T_1 values. Thus, these VOIs were selected for analysis of R1 data in the phantom. Two additional spheres with defined PD values were included for the analysis of the PD data. The reference values of the selected spheres were T1-1 = 1,883.97 ms ($R1 = 0.531\ s^{-1}$), T1-2 = 1,330.16 ms ($R1 = 0.752\ s^{-1}$), T1-3 = 987.27 ms ($R1 = 1.013\ s^{-1}$), T1-4 = 690.08 ms ($R1 = 1.449\ s^{-1}$), PD-3 = 15.01 p.u., and PD-11 = 68.55 p.u. at 20°C (NIST, 2020).

2.8. Quantitative evaluations

For each imaging session and acceleration, the R1, R2*, PD, and MTsat parameter values of the *in vivo* data were determined within the common whole-brain GM and WM segments, within the common GM voxels of the thalamus, and within the common WM voxels of the ACR. For each VOI, histograms of individual quantitative parameter values

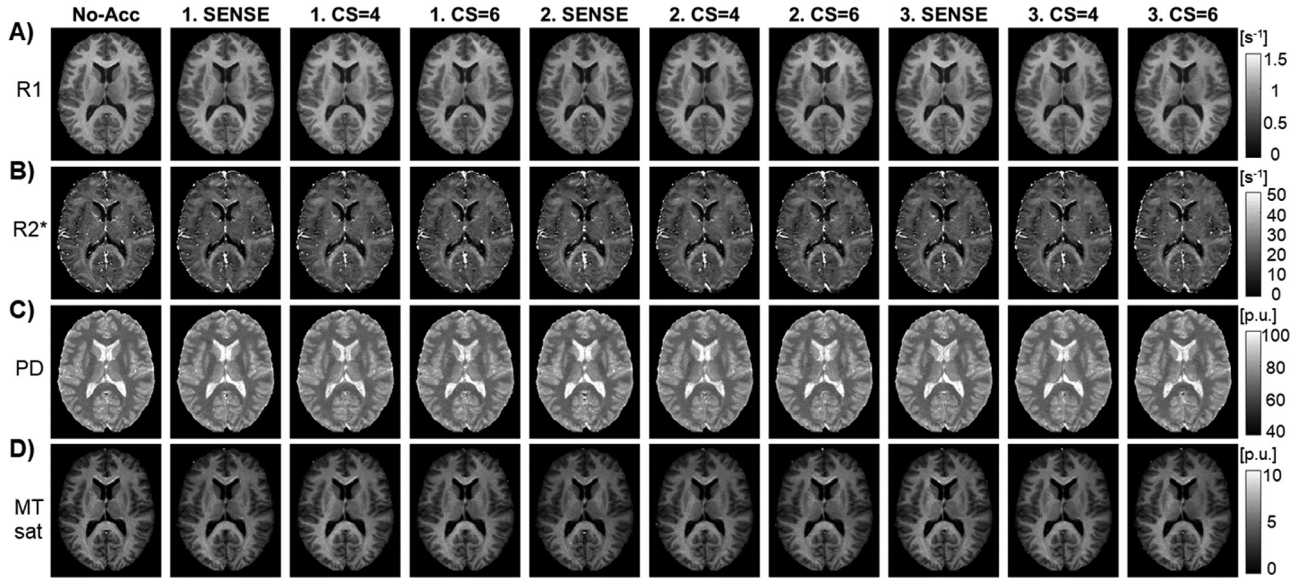

Fig. 2. Representative quantitative parameter maps of all accelerations and scan sessions. R1 (A), R2* (B), PD (C), and MTsat (D) maps are shown for the non-accelerated sequence and the three repetitions of the sequences accelerated with SENSE = 2.5, CS = 4, and CS = 6 (columns).

pooled across participants and boxplots of participant-mean parameter values were compared between imaging accelerations and scan sessions.

Bland-Altman analysis was used to compare quantitative parameter values derived from data accelerated with SENSE = 2.5, CS = 4, and CS = 6 with values derived from non-accelerated data for all participants and for each of the four volumes-of-interest. For each contrast and each accelerated scan, the average difference and the 95% limits of agreement with the non-accelerated scan were determined.

Coefficients of variation (CoV) maps were calculated for each quantitative parameter x across two factors: 1) the three scan sessions using the same imaging accelerations ("repeatability"), and 2) across the three accelerated sequences within the same session ("reproducibility" across different acceleration parameters). For each of the six conditions (SENSE = 2.5, CS = 4, CS = 6, Scan A, Scan B, Scan C), the CoV maps were calculated as

$$CoV = \frac{\sqrt{\frac{1}{3}\left((x_1 - \bar{x})^2 + (x_2 - \bar{x})^2 + (x_3 - \bar{x})^2 \right)}}{\frac{1}{3}(x_1 + x_2 + x_3)}.$$

Here, x_1, x_2, and x_3 are the parameter values in a specific voxel in the three different parameter maps of each condition and $\bar{x}$ is the average value (mean of the three values) within this voxel. From the CoV maps, the average CoV values were determined within the four common volumes-of-interest.

For the phantom scans, CoV maps of R1 and PD data were calculated after registration of all data sets via MATLAB's "imregtform" function to the non-accelerated PD map of the first scan session. The average CoV values were determined within the selected VOIs with defined R1 and PD values (as detailed in section 2.7). Additionally, signal-to-noise ratios (SNR) were determined in the selected VOIs of the R1 and PD data. The SNR was determined as the ratio of the mean and the standard deviation of parameter values across all voxels within a specific VOI.

2.9. Statistical analysis

Repeated measure analyses of variance (ANOVAs) were performed on the *in vivo* data using SPSS (IBM Corp. Released 2019. IBM SPSS Statistics for Windows, Version 26.0. Armonk, NY; RRID: SCR_019096) to test if the imaging acceleration had a statistically significant effect on the quantitative parameter values. For these analyses, the VOI-average parameter values calculated for SENSE = 2.5, CS = 4, and CS = 6 were averaged over the three repeated measures (Scans A-C). The VOI-average parameter values acquired with the non-accelerated sequence were used without any averaging. For each quantitative parameter and each of the four VOIs, these four data sets were included in the ANOVA and the assumption of sphericity was tested using Mauchly's Test of Sphericity. To identify the pair(s) of acceleration methods that resulted in significantly different parameter values, the combinations of parameters and VOIs for which a significant difference (p-value < 0.05) was found were additionally compared using paired two-tailed *t*-tests.

3. Results

3.1. Overall appearance of parameter maps

Quantitative parameter maps that were acquired with various imaging accelerations and in various scan sessions appeared visually very similar (Fig. 2). There seemed to be the same level of detail and comparable contrast between anatomical structures in maps of the same quantitative parameters (Fig. 2). For one volunteer, a SENSE unfolding artifact was present in one of the three data sets accelerated with SENSE (Supplementary Fig. S1). In the same scan session of the same volunteer, artifacts were also seen in the data set accelerated with CS = 6 (Supplementary Fig. S1).

To better illustrate differences between the imaging accelerations and scan sessions, difference images between the parameter maps of the non-accelerated and all accelerated scans were calculated and averaged across participants (Fig. 3). Additionally, average maps of absolute differences were calculated to identify variability between individual measurements (Supplementary Fig. S2).

Generally, PD maps show smaller average percentage differences between accelerated and non-accelerated data compared to R1, R2*, and MTsat. For all contrasts, the subject-average percentage differences to the non-accelerated data is comparable across imaging accelerations (Fig. 3). However, on an individual (i.e., per participant) basis, stronger variations have been found across imaging accelerations, independent of the acceleration method (Supplementary Fig. S3).

3.2. Quantitative evaluation of parameter values

VOI-average quantitative parameter values of R1, R2*, PD, and MTsat were comparable across imaging accelerations and scan sessions in

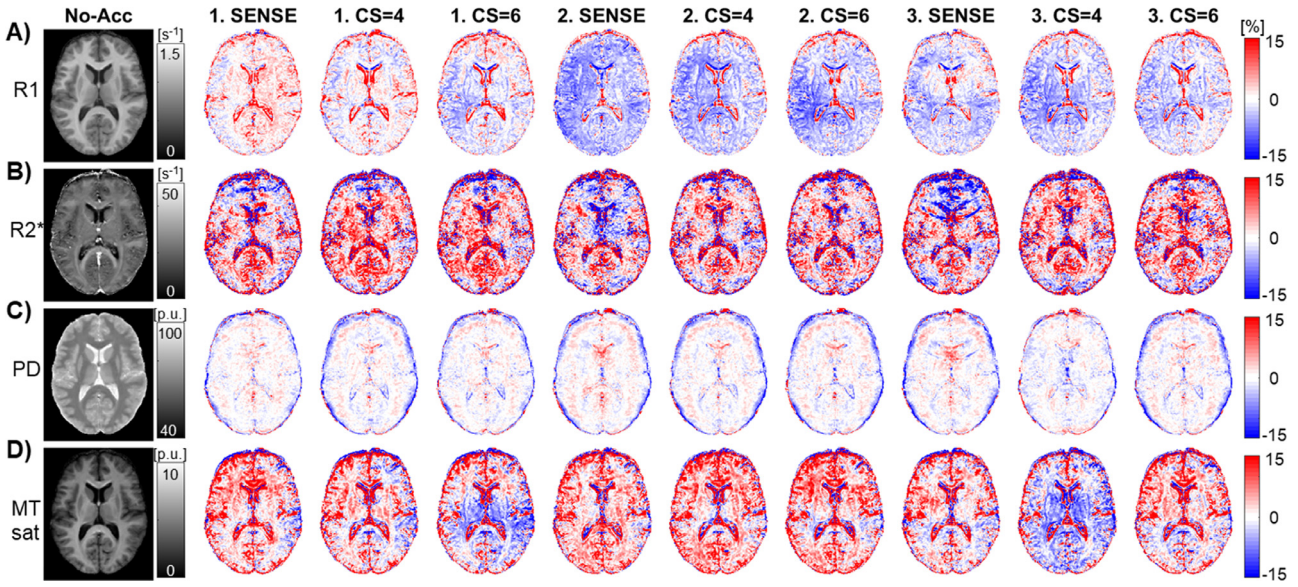

Fig. 3. Subject-average of non-accelerated parameter maps together with their subject-average differences to quantitative parameter maps from all accelerated sequences and scan sessions. The subject-average of non-accelerated reference images of R1 (A), R2* (B), PD (C), and MTsat (D) are shown in the first column. Difference maps were calculated between the non-accelerated reference image and the three repetitions of the sequences accelerated with SENSE = 2.5, CS = 4, and CS = 6 and averaged across all participants (second column to last column). Differences are given in percent deviations from the non-accelerated data.

the four investigated VOIs (Fig. 4). For the interested reader, we provide the same evaluations for three additional WM VOIs in the supplementary material, namely the corpus callosum, the superior corona radiata, and the external capsule and compare those to the values from the ACR (Supplementary Fig. S4). Some parameters varied across imaging accelerations in individual VOIs (e.g., R2* in the ACR). More often, however, VOI-average parameter values varied more strongly across scan sessions (e.g., the mean value of R1 in white matter VOIs or the variance between volunteers of MTsat values in whole-brain WM). Overall, similar variability was observed across both different imaging accelerations and scan sessions (Fig. 4).

Accordingly, for most combinations of quantitative parameters and investigated VOIs, repeated measures ANOVAs did not reveal significant differences between average parameter values acquired with either no acceleration or the three imaging accelerations (Supplementary Table S5). A significant within-subjects effect of the imaging acceleration was only found in two of the 16 VOI-parameter combinations, namely for PD within the thalamus and for R2* in the ARC VOI (Supplementary Table S5). For the VOI-parameter combinations that showed a significant effect of the acceleration method on the VOI-average parameter values, paired *t*-tests were performed using data acquired with various accelerations (Supplementary Table S6).

Similarly, histograms of all individual quantitative parameter values within GM and WM VOIs across participants revealed slight differences between acceleration methods or scan sessions, but generally confirmed a good agreement of pooled mean and standard deviation values across data sets (Supplementary Fig. S7).

Parameter values derived from accelerated and non-accelerated measurements agreed well (Fig. 5). CS-accelerated and SENSE-accelerated data revealed a comparable agreement with non-accelerated data, in particular for R1, PD, and MTsat (Fig. 5A and C-D). In addition, the CS-accelerated and non-accelerated data showed the same or a smaller range of differences (smaller 95% confidence interval) for R1, R2*, and MTsat compared to SENSE-accelerated and non-accelerated data (Fig. 5A-B and D).

In the phantom data, four VOIs with physiological T_1 values were selected for quantitative analysis. Within these VOIs, R1 values showed a very high agreement between non-accelerated data and each of the three accelerated data sets, with an average difference close to zero (Supplementary Fig. S8A). However, the measured R1 values within the four VOIs were increased (by 7.9% for T1-1, 13.8% for T1-2, 19.0% for T1-3, and 16.1% for T1-4) compared to the reference values. For the PD data, two additional VOIs with defined PD values were included in the analysis. Similar to the R1 data, the PD data revealed a good agreement between non-accelerated and accelerated scans (Supplementary Fig. S8B). Additionally, the measured PD values agreed well with the reference values. R2* and MTsat values have not been analyzed since the phantom did not contain any reference values for these parameters and lacked appropriate artifact-free regions with physiological R2* and MTsat values.

In most VOIs of the R1 phantom data, signal-to-noise ratios of the parameter maps tended to be slightly higher in the SENSE = 2.5 and CS = 4 scans compared to CS = 6 or non-accelerated scans (Supplementary Fig. S9A). In the VOIs investigated for PD phantom data, SNR values were usually highest in the CS = 4 data and lowest in the non-accelerated data (Supplementary Fig. S9B). However, mean SNR values were generally similar across acceleration methods and varied between 20 and 32 in both R1 and PD data.

3.3. Coefficients of variation

Subject-average maps of coefficients of variation calculated from data acquired with the same imaging acceleration across different scan sessions (“repeatability”) had a high visual similarity to CoV maps calculated from data acquired within the same scan session using different imaging accelerations (“reproducibility”) (Fig. 6). CoV maps of different parameters varied in their visual appearance: PD values showed the lowest CoV values (darkest CoV maps) while R2*-based CoV maps appeared noisiest (Fig. 6).

For each condition (SENSE = 2.5, CS = 4, CS = 6, Scan A, Scan B, Scan C), VOI-average CoV values were calculated for each participant and contrast (Fig. 7). Repeatability-based CoV values (blue asterisks) were highly comparable to reproducibility-based CoV values (green asterisks) with their mean values ranging between ~2% (PD) and up to

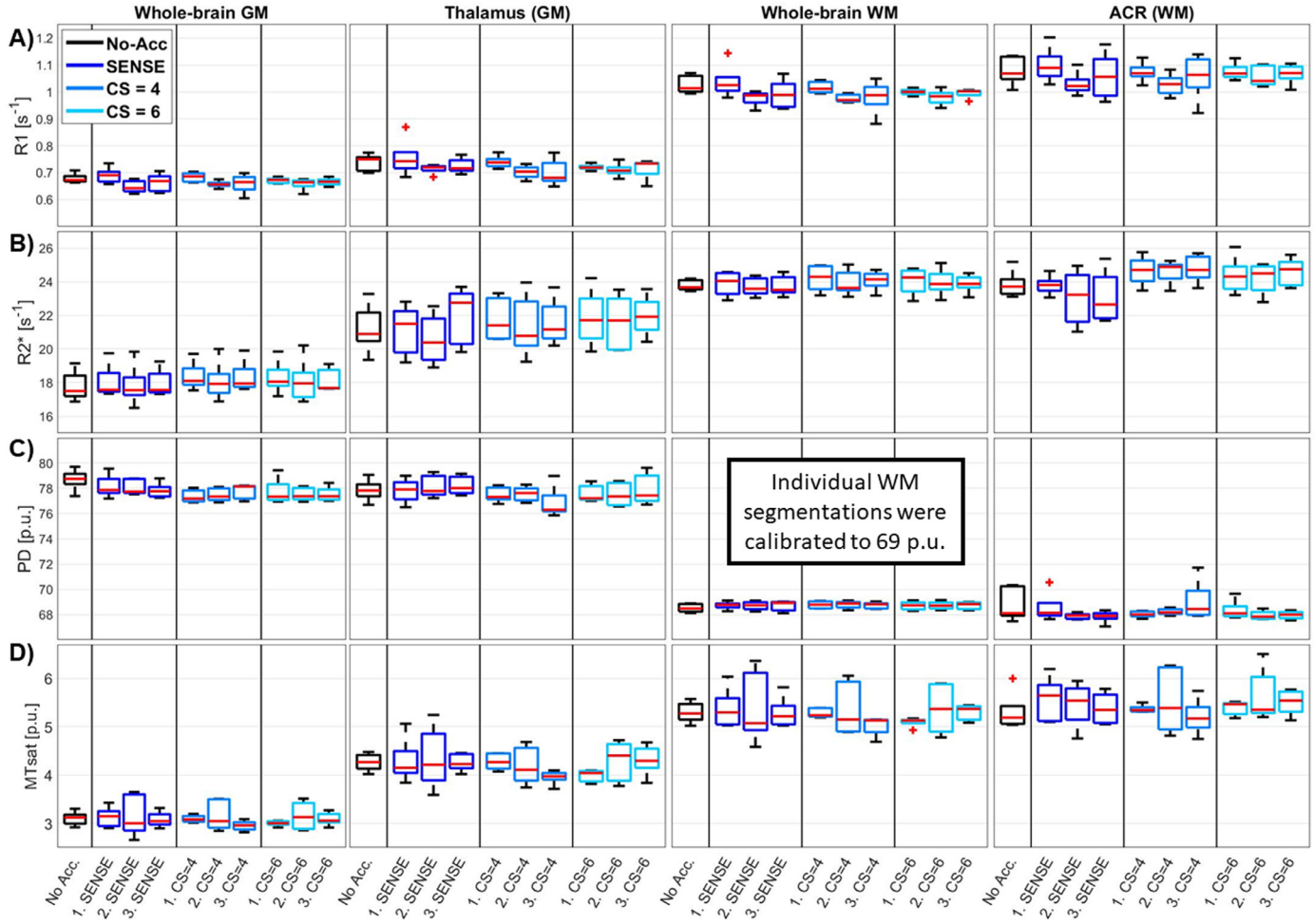

Fig. 4. Boxplots of average quantitative parameter values within GM and WM VOIs across subjects. The VOI-average values of R1 (A), R2* (B), PD (C), and MTsat (D) are shown for whole-brain GM (1st column) and WM (3rd column) segmentations and for common voxels within the thalamus (2nd column) and the anterior corona radiata (4th column). The thalamus VOI comprised 10,300 and the anterior corona radiata 13,000 voxels. Common whole-brain GM and WM segments comprised 443,300 and 389,900 voxels, respectively. The red line represents the median, the edges of the box indicate the 25th and 75th percentiles, the whiskers extend to the most extreme data points not considering outliers, and red +-symbols represent outliers.

~7% (R2*). For most VOIs and contrasts, the mean repeatability-based CoV value (average of blue data points) was slightly higher than the mean reproducibility-based CoV value (average of green data point). This was seen in all VOIs of the R1 and MTsat data and in most VOIs of the R2* and PD data (Fig. 7).

From the phantom data, mean CoV values were calculated in analogy to the *in vivo* data: The repeatability-based CoV values were calculated from the three repeated measures of the protocol with the same acceleration (for the non-accelerated and all accelerated protocols), and the reproducibility-based CoV values from the three accelerated protocols (SENSE = 2.5, CS = 4, and CS = 6) of the same scan session (Supplementary Fig. S10). In the phantom, mean CoV values of the R1 data were slightly lower compared to the *in vivo* data ranging between 1.7% and 3.0%, and CoV values of the PD data were comparable within the two VOIs with calibrated PD values varying between 0.85% and 2.6% (Supplementary Fig. S10). The CoV values of the phantom data showed consistently higher mean repeatability-based than mean reproducibility-based CoV values. This was found in both R1 and PD data and was most prominent in the PD-based CoV values of all VOIs selected from the fiducial spheres with defined T_1 values (Supplementary Fig. S10B). When including the data of the non-accelerated protocol in the calculation of the reproducibility-based CoV values (using four instead of three data sets for the CoV map calculation), the difference between repeatability- and reproducibility-based CoV values decreased, but the overall trend was still visible (not shown).

4. Discussion

This study aimed to investigate the reproducibility of multi-parameter quantitative mapping of R1, R2*, PD, and MTsat comparing a non-accelerated protocol and three different accelerated imaging protocols in five healthy volunteers and in a phantom. Quantitative parameter maps showed similar variability in the visual appearance and in VOI-average evaluations comparing data acquired with various imaging accelerations and across different scan sessions. SNR analyses in selected R1 and PD VOIs of the phantom data revealed comparable SNR across acceleration methods. VOI-average parameter values correlated well between non-accelerated and accelerated scans in both *in vivo* and phantom data. The agreement between parameter values derived from accelerated and non-accelerated scans was very high and comparable across acceleration methods. The reproducibility and repeatability of the measured quantitative parameters were additionally investigated using coefficients of variation. Mostly, mean repeatability-based CoV values were slightly higher than mean reproducibility-based CoV values. This was seen in all R1 and PD VOIs of the phantom and in most VOIs and contrasts of the *in vivo* data.

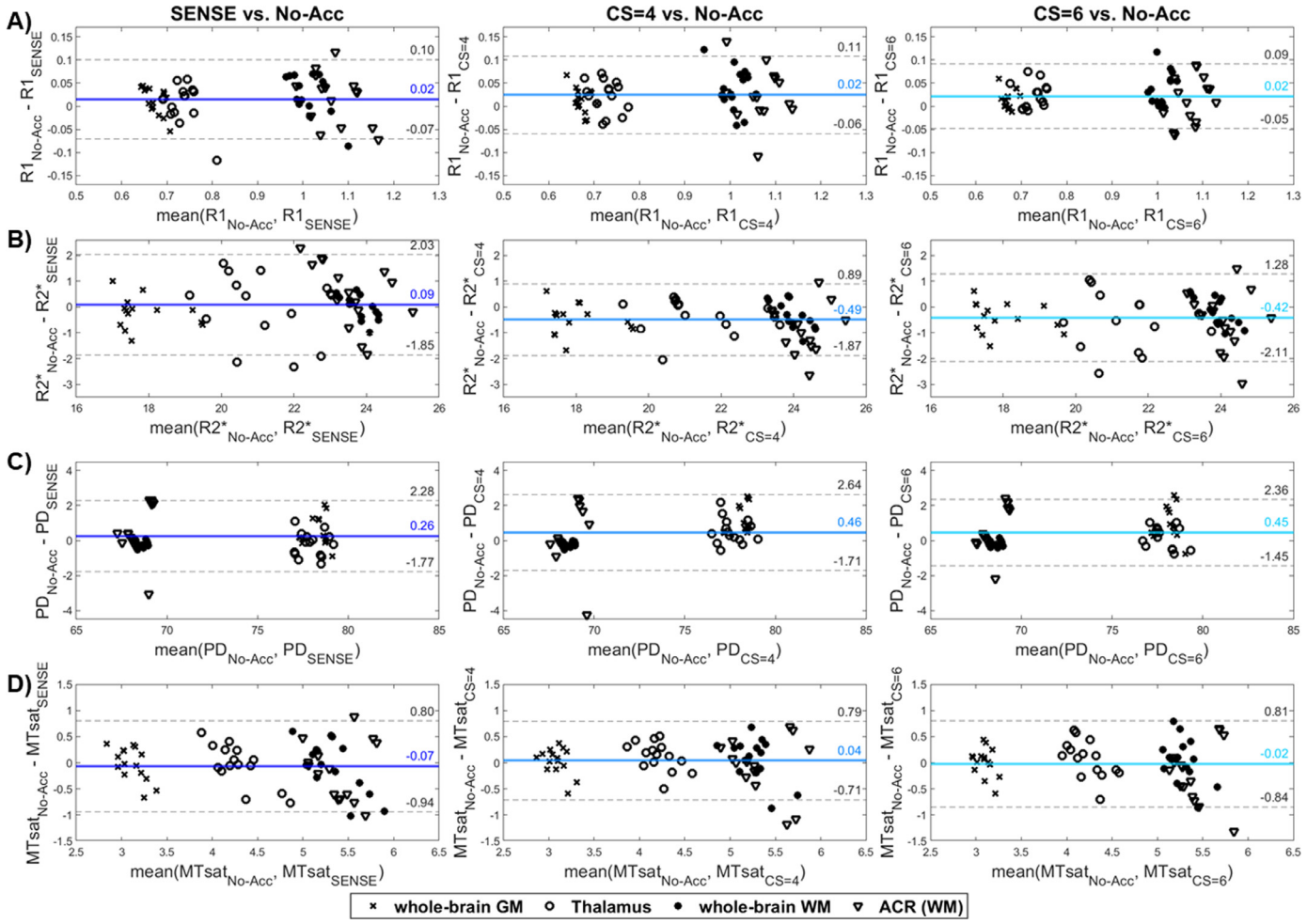

Fig. 5. Bland-Altman plots comparing VOI-average quantitative parameter values between non-accelerated and accelerated data using either SENSE = 2.5, CS = 4, or CS = 6 (columns). The VOI-average parameter values of R1 in s^{-1} (A), $R2^*$ in s^{-1} (B), PD in p.u. (C), and MTsat in p.u. (D) from the three repeated accelerated measurements were compared with the data from the non-accelerated parameter maps. The data of all five participants and four volumes-of-interest were included in the evaluation. Average difference values (blue lines) and 95% limits of agreement (average difference ± 1.96 standard deviations of differences, dashed lines) are provided.

4.1. Quality of parameter maps

Generally, quantitative parameter maps derived from all accelerated and the non-accelerated data showed comparable image quality and level of anatomical detail. However, SENSE unfolding artifacts were found in one data set acquired with SENSE acceleration. CS artifacts were visible in the corresponding CS = 6 data set of the same volunteer and the same scan session but were much less prominent. Thus, parameter maps from data acquired with Compressed SENSE appeared visually equivalent in artifact-free data, but superior to SENSE-accelerated data in case of subject motion. This fits with previous studies that demonstrated high image quality of CS-accelerated MRI for diagnostic imaging (Eichinger et al., 2019; Nam et al., 2019; Vranic et al., 2019). However, some differences were found between imaging acceleration methods with respect to the degree of deviation from the non-accelerated data. The data sets that showed largest deviations varied for each participant and were independent of the acceleration method and acceleration factor but occurred most often in the later acquisitions of each scan session. One reason for this could be an increasing tendency for subject motion over time with an additional dependence on the pre-scans. Both SENSE and Compressed SENSE use pre-scans to obtain coil sensitivity information for reconstructing the accelerated images. In our study, these pre-scans were only performed once at the beginning of each scan session. The last sequence of each session was acquired about 40 minutes later. Thus, head movement of the participants occurring after the pre-scans would have influenced the image quality of the later sequences of each scan session more strongly and could have caused some artifacts independent of the imaging acceleration. This assumption is in line with previous studies highlighting the effect of inter-scan head movement on R1 quantification (Balbastre et al., 2021; Papp et al., 2016) and other MRI methods (Faraji-Dana et al., 2016; Poblador Rodriguez et al., 2021) if the sensitivity of the receive coil is not accurately accounted for. Additionally, this effect most likely also influenced the quality of the non-accelerated data that were used as reference. The total scan duration of the non-accelerated protocol (45 minutes) was quite long making both inter- and intra-scan participant movement more likely, which can cause clearly reduced image quality.

4.2. Accuracy of parameter values

In order to evaluate the accuracy of the measured quantitative parameter values, the *in vivo* data (Fig. 4) were compared to literature values of gray and white matter (Table 1), and the phantom data (Supplementary Fig. S8) were correlated with the given reference values in the selected fiducial spheres.

Quantitative R1 values can depend on the method used for R1 mapping (e.g., inversion recovery or variable flip angle) and the correction methods applied to adjust for confounding factors such as sequence

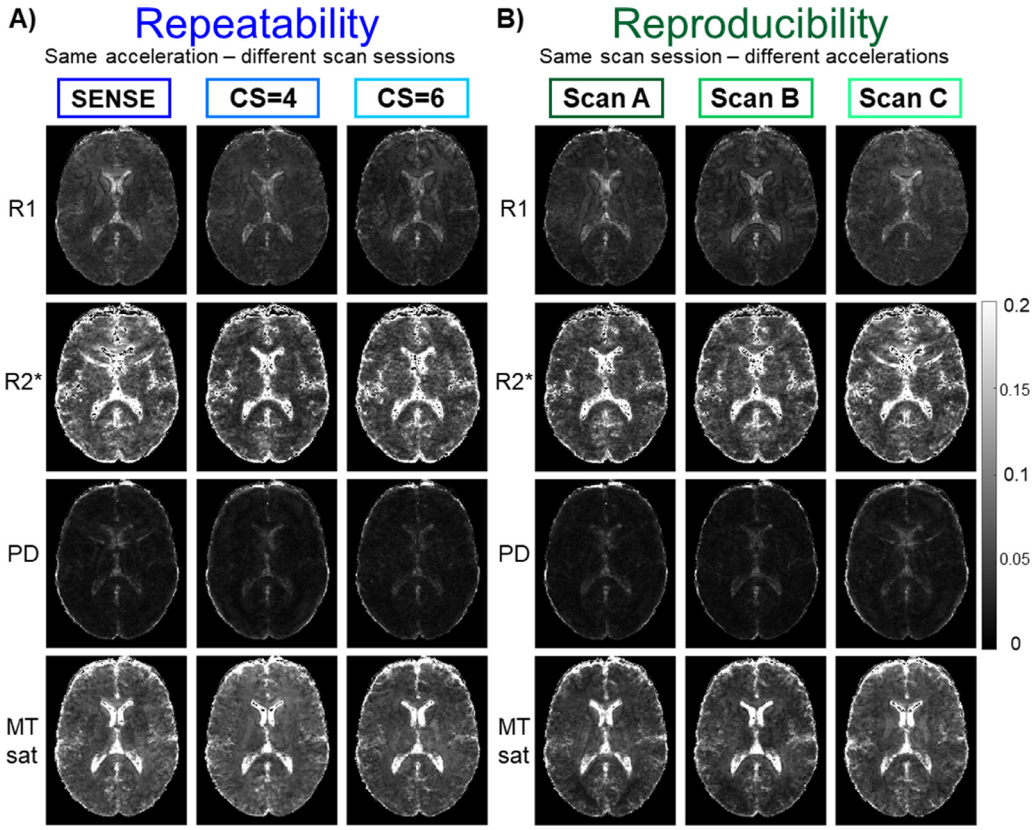

Fig. 6. Subject-average maps of coefficients of variation (CoV). In A), CoV maps were calculated from the three scans with the same acceleration method (repeatability) and then averaged across subjects. In B), CoV maps were calculated from the three measurements within the same scan session and with different accelerations (reproducibility) and also averaged across subjects.

Table 1
Quantitative parameter values of R1, R2*, PD, and MTsat in whole-brain GM and WM found in this study compared to literature values from previous studies. T_1 and $T_2{}^*$ values from literature were converted to R1 and R2* values via $T_1 = 1/R1$ and $T_2{}^* = 1/R2^*$, respectively. Literature PD values were either provided as proton density values or water content.

Parameter	GM regions		WM regions		References
	This study	Literature	This study	Literature	
R1 [s^{-1}]	0.67 ± 0.02	0.61 – 0.75	1.00 ± 0.04	1.04 – 1.22	(Gelman et al., 2001; Preibisch and Deichmann, 2009; Wansapura et al., 1999; Weiskopf et al., 2013; Wright et al., 2008)
R2* [s^{-1}]	18.1 ± 0.9	15 – 24	23.9 ± 0.6	18.9 – 22.4	(Krüger et al., 2001; Peters et al., 2007; Wansapura et al., 1999; Weiskopf et al., 2013)
PD [p.u.]	77.8 ± 0.7	78 – 84.4	68.7 ± 0.3	68.3 – 70	(Farace et al., 1997; Gutteridge et al., 2002; Weiskopf et al., 2013)
MTsat [p.u.]	3.09 ± 0.21	0.8 – 2.25	5.28 ± 0.37	1.7 – 4.8	(Hagiwara et al., 2018; Helms et al., 2008; Leutritz et al., 2020; Lommers et al., 2019; Weiskopf et al., 2013)

parameters, hardware components, or tissue properties (Stikov et al., 2015). Moreover, the use of a single R1 value in brain tissue is a significant simplification of the multiple compartments and complex tissue structure (Labadie et al., 2014), adding to variations between acquisition methods inadvertently probing different tissue aspects (Weiskopf et al., 2021). For the VFA method applied in this study, the most important confounding factors are deviations of the real flip angle from the nominal flip angle, insufficient RF spoiling, and inadvertent MT effects (Teixeira et al., 2019). The first two effects were corrected via B1 mapping with the actual flip angle imaging method (Yarnykh, 2007) and using imperfect spoiling correction (Baudrexel et al., 2018), respectively. However, correcting for inadvertent MT effects would have required tuning the RF pulse duration for each sequence separately, which would be rather cumbersome and error-prone or would require pulse sequence programming on the MR scanner platform used in this study. The mean R1 values obtained in this study were 0.67 ± 0.02 s^{-1} in whole-brain GM and 1.00 ± 0.04 s^{-1} in whole-brain WM, which are in good accordance with literature values of R1 or T_1 (=1/R1) found in previous studies (Table 1). Similarly, mean R2* in whole-brain GM (18.1 ± 0.9 s^{-1}) and WM (23.9 ± 0.6 s^{-1}) approximately conform to literature values (Table 1). R2* values can be affected by magnetic background fields or rather by the quality of the shim and by paramagnetic (iron) accumulations in the tissue. Even though we excluded brain regions with strong artifacts and extremely high R2* values, our results are most likely still influenced by these confounding factors leading to a higher variance and slightly increased R2* values. Since the hMRI toolbox calibrates PD data to an average value of 69 p.u. in whole-brain WM, the mean PD values in white matter (68.7 ± 0.3 p.u.) are in perfect agreement with literature values. In whole-brain GM, the PD values were 77.8 ± 0.7 p.u., which agree well with the literature values of PD or water content (Table 1). For the MTsat, a comparison with reference values is more complicated since MTsat is influenced by detailed properties of the magnetization transfer RF pulse, i.e., primarily the effective RF saturation power determined by the MT flip angle, the off-resonance frequency,

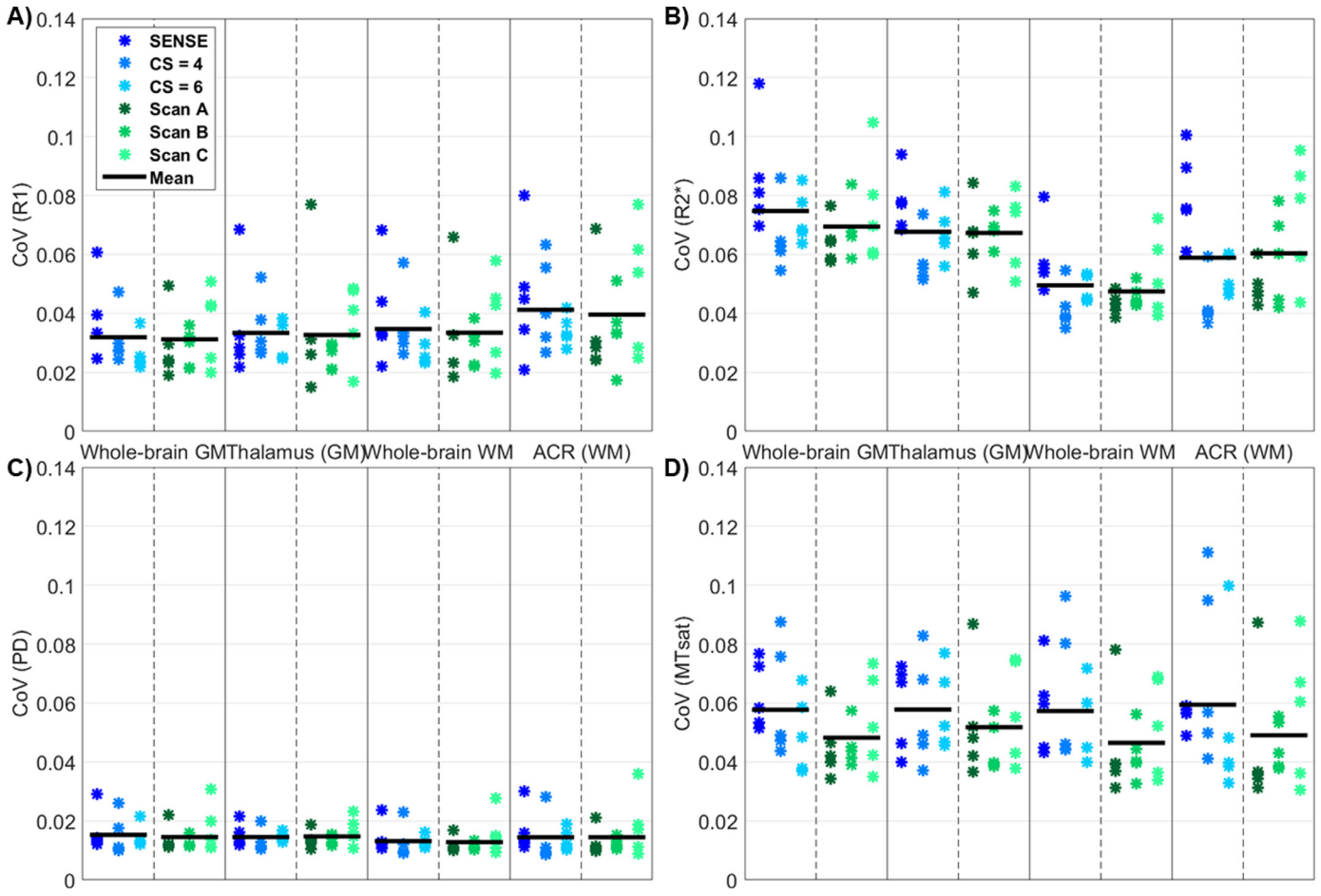

Fig. 7. Coefficients of variation (CoV) of the quantitative parameter maps from the repeatability (blue) and reproducibility (green) measurements. In each panel, the VOI-average CoV values of R1 (A), R2* (B), PD (C), and MTsat (D) are shown for whole-brain GM, the thalamus, whole-brain WM, and the anterior corona radiata (ACR). The mean of the fifteen values per factor ("repeatability" or "reproducibility") is represented with a black line for each parameter and volume-of-interest.

the MT pulse duration, as well as TR (Teixeira et al., 2019). The whole-brain MTsat values of this study were 3.09 ± 0.21 p.u. in GM and 5.28 ± 0.37 p.u. in WM, which are clearly higher than the literature values (Table 1). These increased MTsat values could be caused by our comparably short MT pulse duration (compared to (Helms et al., 2008) and (Hagiwara et al., 2018)) and, generally, a lower MT saturation frequency (resulting in higher direct saturation) or a different pulse shape.

In the phantom, reference values were only available for R1 and PD data. Since all PD values derived from phantom data were calibrated to the fiducial sphere that was designed to have a PD value of 68.55 p.u. ("PD-11"), it is not surprising that PD values from this VOI perfectly agreed with the expected reference value. The second PD-calibrated VOI ("PD-3") also showed good agreement with the expected reference value (average deviation 10.3%). For most of the selected R1-calibrated VOIs (with physiological R1 values), the measured R1 values slightly deviated from the reference values. The VOI with the lowest reference R1 value (R1 = 0.531 s^{-1}) showed the best accordance with the measured R1 value. For VOIs with higher reference R1 values, the measured R1 values were increased compared to the expected reference value by up to 19% (Supplementary Fig. S8). Here, the most likely explanation is that these VOIs exhibited non-physiological T_2 values of ~520 – 1,490 ms, resulting in significant residual transverse coherences despite RF spoiling. The hMRI toolbox corrects R1 for imperfect RF spoiling based on simulations of the steady-state signal for a given phase increment (Preibisch and Deichmann, 2009). However, it cannot adequately correct the R1 values in the phantom because underlying simulations used a T_2 value of 64 ms (https://github.com/hMRI-group/hMRI-toolbox/wiki/DefaultsAndCustomization, accessed on December 14, 2021), which is physiologically plausible at 3 T but about an order of magnitude lower than the actual T_2 values of the phantom. Such a T_2-dependence in the estimated T_1 data has already been highlighted and quantified in previous studies at 3 T (Baudrexel et al., 2018; Heule et al., 2016) and at 7 T (Corbin and Callaghan, 2021). A previous study that did not perform any correction for imperfect RF spoiling has found even greater deviations between the measured T_1 and the reference T_1 values when using the variable flip angle method for T_1 mapping (Keenan et al., 2016).

4.3. Precision of parameter values

Precision describes the variability of test results determined in independent measurements of the same quantitative parameter (Taylor and Kuyatt, 1994). It can be assessed, e.g., in repeatability studies via repeated measures of the same condition or in reproducibility studies utilizing different conditions to obtain the same physical quantity (Sullivan et al., 2015).

Here, precision was assessed using repeatability- and reproducibility-based coefficients of variation and by calculating signal-to-noise ratios in several VOIs of the phantom data.

Both reproducibility-based and repeatability-based CoV values of all quantitative parameter values in the *in vivo* data agree well with intra-site CoV values from a previous study (Leutritz et al., 2020). Further-

more, the phantom CoV values of R1 are in line with CoV values from a multi-vendor repeatability study using the same phantom with CoV values ranging between 0-5% for most vendors (Keenan et al., 2016).

Overall, our CoV values showed similar precision when comparing quantitative parameter values from either different imaging accelerations or different scan sessions. This was reflected in visually highly comparable CoV maps for individual parameters (Fig. 6). Interestingly, in most VOIs, average quantitative parameter values were more comparable (lower average CoV values) across various types of accelerations than across scan sessions (Fig. 7 and Supplementary Fig. S10), indicating a high reproducibility of the parameter values using various imaging accelerations. In addition, repeatability-based CoV values from CS = 4 and CS = 6 acquisitions were generally lower compared to CoV values of SENSE = 2.5 (Fig. 7A-C), suggesting a slightly higher precision in quantitative parameter maps acquired with Compressed SENSE.

These findings were supported by the signal-to-noise analyses in the selected R1 and PD VOIs of the phantom data. Compared to the non-accelerated protocols, the accelerated protocols showed a comparable level of noise in the quantitative parameter maps and resulted in similar or slightly increased signal-to-noise ratios (Supplementary Fig. S9), suggesting a high precision of accelerated multi-parameter mapping. The effect of various imaging accelerations on the noise level in T_1-weighted images has already been investigated in a previous study (Yarach et al., 2021), showing no statistical difference between the SNR using SENSE = 2 and CS = 4, in line with our findings. A reason for the comparable SNR, despite the shorter scan duration, could be the regularization procedures applied by the acceleration methods, especially the additional regularization to reduce noise implemented in Compressed SENSE (Geerts-Ossevoort et al., 2018). Although we did not find reduced accuracy in our accelerated MPM measurements of healthy participants, regularization procedures generally increase precision at the expense of accuracy. Especially in pathologies, a lower accuracy of MPM could result in lower sensitivity to abnormal tissue changes. While investigating the sensitivity of MPM to pathological alterations or physiological effects was outside the scope of this study, a potentially reduced contrast-to-noise in parameter maps acquired with CS cannot be fully excluded for clinical applications.

4.4. Reproducibility using Compressed SENSE

Overall, the measured quantitative parameter values depended neither on imaging acceleration in general (non-accelerated vs. accelerated protocols), nor on acceleration techniques (SENSE vs. CS) or acceleration factor (CS = 4 vs. CS = 6) in particular. Especially for the *in vivo* data, R1, R2*, and PD values agreed well with the literature, showing high accuracy of all MPM protocols, independent of the presence and type of acceleration method.

Furthermore, the agreement between accelerated and non-accelerated parameter maps was found to be high for all imaging accelerations. Compared to the SENSE-accelerated data, the data accelerated with CS = 6 even showed a smaller range of differences (95% confidence interval) and thus a higher correlation to the non-accelerated data for all contrasts (Fig. 5). This suggests that Compressed SENSE is more favorable for accelerating MPM protocols compared to the conventional SENSE acceleration. One possible explanation for this observation might be the more favorable artifact behavior of CS acceleration, at least in compliant subjects where motion is not a real problem. In agitated patient populations, however, more severe artifacts have also been observed with CS (Sartoretti et al., 2018).

The analysis of CoV values revealed a comparable or even lower variability of quantitative parameter values acquired with different acceleration methods compared to parameter values acquired in multiple scan sessions (at different time points) using identical imaging protocols. In combination with the comparable level of noise of parameter maps derived from all phantom data sets, this demonstrates the high precision of all investigated accelerated multi-parameter mapping protocols. Thus, the results of this study suggest that MPM is highly reproducible using different imaging accelerations, including Compressed SENSE with acceleration factors up to CS = 6. These findings are in good accordance with previous studies investigating the impact of CS acceleration on other imaging sequences (Eichinger et al., 2019; Nam et al., 2019; Vranic et al., 2019).

4.5. Limitations

The different scan sessions of the *in vivo* measurements were several months apart, a period long enough to enable changes in the brain structure and volume, e.g., due to the hydration state (Streitbürger et al., 2012), learning (Driemeyer et al., 2008; Hofstetter et al., 2013), or even aging (Fjell and Walhovd, 2010), and thus to possibly affect quantitative structural parameters. However, similar differences between VOI-average quantitative parameter values were found in the phantom data that cannot be prone to plastic and physiological alterations and have been measured only a few days apart. Thus, effects from structural alterations of the brain tissues do not seem to be prominent. Additionally, the strength of the magnetic field and thus the imaging frequency show a slight drift over time, which can affect parameter quantification. The largest difference in imaging frequencies found among *in vivo* scans in this study was 3.7 ppm resulting in a possible frequency-dependent R1 variation of about 1.5% (assuming $T_1 \sim B^{1/3}$ (Bottomley et al., 1984)). However, this effect is rather small compared to the R1 fluctuations of more than 20% found in the investigated volumes-of-interest in this study. Another limitation of this study is that the pre-scans were only performed once at the beginning of each scan session, which most likely affected the image quality of the later protocols of each session. For future studies, we recommend repeating the pre-scans before each protocol. Furthermore, signal-to-noise evaluations based on a single image could only be performed in the phantom data, since the *in vivo* data were lacking sufficiently large homogeneous brain regions without anatomical structure or physiological “noise”.

For multi-parameter mapping, we used the hMRI toolbox, which is optimized for brain data. This means that calculation of quantitative parameter maps was based on several assumptions that are met in human brain scans but can be violated in phantoms. A few processing parameters could be adjusted to improve the processing of our phantom data, but others were fixed by the toolbox, such as certain constants that serve as input for simulations and correction procedures. One example here is the T_2 value of the scanned sample, which is needed for calculating the correction factors for insufficient RF spoiling. However, the phantom’s T_2 values deviated strongly from physiological values with some of them more than ten times greater than T_2 values of GM or WM. This discrepancy between simulated and actual physiological properties presumably confounded the calculation of quantitative parameter maps and possibly affected the signal-to-noise ratios. Therefore, future studies should compare the variability and noise levels between non-accelerated and accelerated MPM protocols in a phantom suitable for MPM using the variable flip angle approach with relaxation rates and proton density values comparable to brain tissue.

In this study, the reproducibility of the MPM protocol accelerated using Compressed SENSE was only investigated on a single MR scanner. However, a previous study already compared the reliability of MPM in a multi-center study and found high reproducibility of quantitative parameter maps across sites, two vendors, and time points (Leutritz et al., 2020). For a more general assessment of the feasibility of Compressed SENSE for MPM, future studies could also investigate the reproducibility of CS-accelerated protocols at several sites and using different scanner models.

5. Conclusion

Compressed SENSE with acceleration factors up to at least 6 enables the acquisition of highly reproducible multi-parameter mapping met-

rics. CS-accelerated MPM using the hMRI toolbox for parameter quantification allows high precision mapping of the quantitative biomarkers R1, R2*, PD, and MTsat. Obtained parameter maps are similarly as accurate as conventional SENSE-accelerated or non-accelerated protocols, while the scan duration of the CS = 6 protocol is almost halved compared to the original SENSE-accelerated scans. Thus, Compressed SENSE can be used to accelerate MPM to clinically feasible scan times without loss of fidelity. CS is thus highly promising for widespread diagnostic applications and facilitates quantitative multi-parameter magnetic resonance imaging in every day clinical routines.

Data and code availability statement

In line with local ethics guidelines and subject privacy policies, the acquired data are only available via a request to the authors. Institutional policies require a formal data sharing agreement. The hMRI toolbox and its source code, which was used for calculation of quantitative parameter maps, is publicly available via the link provided in the methods section. The latest version of the hMRI toolbox is available from hMRI.info.

Funding information

Ronja Berg is supported by a Ph.D. grant from the Friedrich-Ebert-Stiftung. Dr. Christine Preibisch received a grant from the German Research Foundation (DFG, grant PR 1039/6-1). Tobias Leutritz has received funding from the European Union's Horizon 2020 research and innovation program under the grant agreement number 681094, and he is supported by the Swiss State Secretariat for Education, Research and Innovation (SERI) under contract number 15.0137. Prof. Dr. Nikolaus Weiskopf was supported by the European Research Council under the European Union's Seventh Framework Programme (FP7/2007-2013) / ERC grant agreement number 616905, and the BMBF (01EW1711A & B) in the framework of ERA-NET NEURON.

Declarations of Competing Interest

The Max Planck Institute for Human Cognitive and Brain Sciences has an institutional research agreement with Siemens Healthcare. NW holds a patent on acquisition of MRI data during spoiler gradients (US 10,401,453 B2). NW was a speaker at an event organized by Siemens Healthcare and was reimbursed for the travel expenses.

Credit authorship contribution statement

Ronja C. Berg: Methodology, Software, Validation, Formal analysis, Investigation, Writing – original draft, Visualization. **Tobias Leutritz:** Methodology, Software, Writing – review & editing. **Nikolaus Weiskopf:** Conceptualization, Writing – review & editing, Supervision, Funding acquisition. **Christine Preibisch:** Conceptualization, Writing – review & editing, Supervision, Funding acquisition.

Acknowledgements

We thank Stephan Kaczmarz (Department for Neuroradiology, TUM) for his advice and discussions during preparatory test scans and analyses, Gabriel Hoffmann (Department for Neuroradiology, TUM) for his support with Philips pulse sequence issues, and Prof. Claus Zimmer (Department for Neuroradiology, TUM) for providing infrastructure, access to the MR scanner, and financial support. Furthermore, we thank Dr. Marion Menzel and Sebastian Endt for providing the NIST/ISMRM system phantom. Finally, we thank our five participants for participating in this study.

Supplementary materials

Supplementary material associated with this article can be found, in the online version, at doi:10.1016/j.neuroimage.2022.119092.

References

Akçakaya, M., Basha, T.A., Chan, R.H., Manning, W.J., Nezafat, R., 2014. Accelerated isotropic sub-millimeter whole-heart coronary MRI: compressed sensing versus parallel imaging. Magn. Reson. Med. 71, 815–822. doi:10.1002/mrm.24683.

Ashburner, J., Friston, K.J., 2005. Unified segmentation. Neuroimage 26, 839–851. doi:10.1016/j.neuroimage.2005.02.018.

Balbastre, Y., Aghaeifar, A., Corbin, N., Brudfors, M., Ashburner, J., Callaghan, M.F., 2021. Correcting inter-scan motion artefacts in quantitative R1 mapping at 7T. arXiv preprint arXiv:2108.10943. https://arxiv.org/abs/2108.10943.

Baudrexel, S., Nöth, U., Schüre, J.R., Deichmann, R., 2018. T1 mapping with the variable flip angle technique: a simple correction for insufficient spoiling of transverse magnetization. Magn. Reson. Med. 79, 3082–3092. doi:10.1002/mrm.26979.

Behrens, T.E., Johansen-Berg, H., Woolrich, M., Smith, S., Wheeler-Kingshott, C., Boulby, P., Barker, G., Sillery, E., Sheehan, K., Ciccarelli, O., 2003. Non-invasive mapping of connections between human thalamus and cortex using diffusion imaging. Nat. Neurosci. 6, 750–757. doi:10.1038/nn1075.

Berg, R., Leutritz, T., Kaczmarz, S., Zimmer, C., Weiskopf, N., Preibisch, C., 2020. Evaluating compressed SENSE acceleration for multi-parametric quantitative mapping of R1, R2*, PD, and MTsat with the hMRI toolbox.

Bottomley, P.A., Foster, T.H., Argersinger, R.E., Pfeifer, L.M., 1984. A review of normal tissue hydrogen NMR relaxation times and relaxation mechanisms from 1–100 MHz: dependence on tissue type, NMR frequency, temperature, species, excision, and age. Med. Phys. 11, 425–448. doi:10.1118/1.595535.

Bottomley, P.A., Hardy, C., Argersinger, R., Allen-Moore, G., 1987. A review of 1H nuclear magnetic resonance relaxation in pathology: are T1 and T2 diagnostic? Med. Phys. 14, 1–37. doi:10.1118/1.596111.

Boyarko, A.C., Dillman, J.R., Tkach, J.A., Pednekar, A.S., Trout, A.T., 2021. Comparison of compressed SENSE and SENSE for quantitative liver MRI in children and young adults. Abdom Radiol. (NY) 46, 1–9. doi:10.1007/s00261-021-03092-x.

Brandhofe, A., Stratmann, C., Schüre, J.-R., Pilatus, U., Hattingen, E., Deichmann, R., Nöth, U., Wagner, M., Gracien, R.-M., Seiler, A., 2020. T2 relaxation time of the normal-appearing white matter is related to the cognitive status in cerebral small vessel disease. J. Cereb. Blood Flow Metab. doi:10.1177/0271678X20972511, 0271678X20972511.

Callaghan, M.F., Freund, P., Draganski, B., Anderson, E., Cappelletti, M., Chowdhury, R., Diedrichsen, J., FitzGerald, T.H., Smittenaar, P., Helms, G., 2014. Widespread age-related differences in the human brain microstructure revealed by quantitative magnetic resonance imaging. Neurobiol. Aging 35, 1862–1872. doi:10.1016/j.neurobiolaging.2014.02.008.

Callaghan, M.F., Mohammadi, S., Weiskopf, N., 2016. Synthetic quantitative MRI through relaxometry modelling. NMR Biomed. 29, 1729–1738. doi:10.1002/nbm.3658.

Candès, E.J., Romberg, J.K., Tao, T., 2006a. Robust uncertainty principles: exact signal reconstruction from highly incomplete frequency information. IEEE Trans. Inf. Theory 52, 489–509. doi:10.1109/TIT.2005.862083.

Candès, E.J., Romberg, J.K., Tao, T., 2006b. Stable signal recovery from incomplete and inaccurate measurements. Commun. Pure Appl. Mathem. 59, 1207–1223. doi:10.1002/cpa.20124.

Cho, S., Choi, Y., Chung, S., Lee, J., Baek, J., 2019. High-resolution MRI using compressed sensing-sensitivity encoding (CS-SENSE) for patients with suspected neurovascular compression syndrome: comparison with the conventional SENSE parallel acquisition technique. Clin. Radiol. 74, 817. doi:10.1016/j.crad.2019.06.023, e819-817. e814.

Cooper, G., Hirsch, S., Scheel, M., Brandt, A.U., Paul, F., Finke, C., Boehm-Sturm, P., Hetzer, S., 2020. Quantitative multi-parameter mapping optimized for the clinical routine. Front. Neurosci. 14, 1290. doi:10.3389/fnins.2020.611194.

Corbin, N., Callaghan, M.F., 2021. Imperfect spoiling in variable flip angle T1 mapping at 7T: Quantifying and minimizing impact. Magn. Reson. Med. 86, 693–708. doi:10.1002/mrm.28720.

Ding, J., Duan, Y., Zhuo, Z., Yuan, Y., Zhang, G., Song, Q., Gao, B., Zhang, B., Wang, M., Yang, L., 2021. Acceleration of Brain TOF-MRA with Compressed Sensitivity Encoding: A Multicenter Clinical Study. AJNR Am. J. Neuroradiol. 42, 1208–1215. doi:10.3174/ajnr.A7091.

Donoho, D.L., 2006. Compressed sensing. IEEE Trans. Inf. Theory 52, 1289–1306. doi:10.1109/TIT.2006.871582.

Driemeyer, J., Boyke, J., Gaser, C., Büchel, C., May, A., 2008. Changes in gray matter induced by learning—revisited. PLoS One 3, e2669. doi:10.1371/journal.pone.0002669.

Duan, Y., Zhang, J., Zhuo, Z., Ding, J., Ju, R., Wang, J., Ma, T., Haller, S., Liu, Y., Liu, Y., 2020. Accelerating brain 3D T1-weighted turbo field echo MRI using compressed sensing-sensitivity encoding (CS-SENSE). Eur. J. Radiol. 131, 109255. doi:10.1016/j.ejrad.2020.109255.

Eichinger, P., Hock, A., Schön, S., Preibisch, C., Kirschke, J.S., Mühlau, M., Zimmer, C., Wiestler, B., 2019. Acceleration of double inversion recovery sequences in multiple sclerosis with compressed sensing. Invest. Radiol. 54, 319–324. doi:10.1097/RLI.0000000000000550.

Farace, P., Pontalti, R., Cristoforetti, L., Antolini, R., Scarpa, M., 1997. An automated method for mapping human tissue permittivities by MRI in hyperthermia treatment planning. Phys. Med. Biol. 42, 2159. doi:10.1088/0031-9155/42/11/011.

Faraji-Dana, Z., Tam, F., Chen, J.J., Graham, S.J., 2016. A robust method for suppressing motion-induced coil sensitivity variations during prospective correction of head motion in fMRI. Magn. Reson. Imaging 34, 1206–1219. doi:10.1016/j.mri.2016.06.005.

Fjell, A.M., Walhovd, K.B., 2010. Structural brain changes in aging: courses, causes and cognitive consequences. Rev. Neurosci. 21, 187–222. doi:10.1515/REVNEURO.2010.21.3.187.

Freund, P., Rothwell, J., Craggs, M., Thompson, A.J., Bestmann, S., 2011. Corticomotor representation to a human forearm muscle changes following cervical spinal cord injury. Eur. J. Neurosci. 34, 1839–1846. doi:10.1111/j.1460-9568.2011.07895.x.

Fujita, S., Hagiwara, A., Takei, N., Hwang, K.-P., Fukunaga, I., Kato, S., Andica, C., Kamagata, K., Yokoyama, K., Hattori, N., 2021. Accelerated isotropic multiparametric imaging by high spatial resolution 3D-QALAS with compressed sensing: a phantom, volunteer, and patient study. Invest. Radiol. 56, 292. doi:10.1097/RLI.0000000000000744.

Geerts-Ossevoort, L., De Weerdt, E., Duijndam, A., van IJperen, G., Peeters, H., Doneva, M., Nijenhuis, M., Huang, A., 2018. Compressed SENSE speed done right. every time. Philips FieldStrength Magazine 2018, 1–16 his publication is available via: https://www.philips.com.vn/c-dam/b2bhc/master/landing-pages/compressed-sense-redesign/speed/MR_white_paper_Compressed_SENSE.pdf.

Gelman, N., Ewing, J.R., Gorell, J.M., Spickler, E.M., Solomon, E.G., 2001. Interregional variation of longitudinal relaxation rates in human brain at 3.0 T: relation to estimated iron and water contents. Magn. Reson. Med. 45, 71–79. doi:10.1002/1522-2594(200101)45:1<71::AID-MRM1011>3.0.CO;2-2.

Grabher, P., Callaghan, M.F., Ashburner, J., Weiskopf, N., Thompson, A.J., Curt, A., Freund, P., 2015. Tracking sensory system atrophy and outcome prediction in spinal cord injury. Ann. Neurol. 78, 751–761. doi:10.1002/ana.24508.

Gutteridge, S., Ramanathan, C., Bowtell, R., 2002. Mapping the absolute value of M0 using dipolar field effects. Magn. Reson. Med. 47, 871–879. doi:10.1002/mrm.10142.

Hagiwara, A., Hori, M., Kamagata, K., Warntjes, M., Matsuyoshi, D., Nakazawa, M., Ueda, R., Andica, C., Koshino, S., Maekawa, T., 2018. Myelin measurement: Comparison between simultaneous tissue relaxometry, magnetization transfer saturation index, and T 1 w/T 2 w ratio methods. Sci. Rep. 8, 1–12. doi:10.1038/s41598-018-28852-6.

Helms, G., Dathe, H., Dechent, P., 2008. Quantitative FLASH MRI at 3T using a rational approximation of the Ernst equation. Magn. Reson. Med. 59, 667–672. doi:10.1002/mrm.21542.

Heule, R., Ganter, C., Bieri, O., 2016. Variable flip angle T1 mapping in the human brain with reduced T2 sensitivity Using fast radiofrequency-spoiled gradient echo imaging. Magn. Reson. Med. 75, 1413–1422. doi:10.1002/mrm.25668.

Hofstetter, S., Tavor, I., Moryosef, S.T., Assaf, Y., 2013. Short-term learning induces white matter plasticity in the fornix. J. Neurosci. 33, 12844–12850. doi:10.1523/JNEUROSCI.4520-12.2013.

Holland, B.A., Haas, D.K., Norman, D., Brant-Zawadzki, M., Newton, T.H., 1986. MRI of normal brain maturation. AJNR Am. J. Neuroradiol. 7, 201–208.

Jaeger, E., Sonnabend, K., Schaarschmidt, F., Maintz, D., Weiss, K., Bunck, A.C., 2020. Compressed-sensing accelerated 4D flow MRI of cerebrospinal fluid dynamics. Fluids Barriers CNS 17, 1–11. doi:10.1186/s12987-020-00206-3.

Just, M., Thelen, M., 1988. Tissue characterization with T1, T2, and proton density values: results in 160 patients with brain tumors. Radiology 169, 779–785. doi:10.1148/radiology.169.3.3187000.

Kaga, T., Noda, Y., Mori, T., Kawai, N., Takano, H., Kajita, K., Yoneyama, M., Akamine, Y., Kato, H., Hyodo, F., 2021. Diffusion-weighted imaging of the abdomen using echo planar imaging with compressed SENSE: feasibility, image quality, and ADC value evaluation. Eur. J. Radiol. 142, 109889. doi:10.1016/j.ejrad.2021.109889.

Keenan, K.E., Stupic, K.F., Boss, M.A., Russek, S.E., Chenevert, T.L., Prasad, P.V., Reddick, W.E., Zheng, J., Hu, P., Jackson, E.F., 2016. Comparison of T1 measurement using ISMRM/NIST system phantom. In: ISMRM 24th Annual Meeting & Exhibition. Singapore.

Kocaoglu, M., Pednekar, A., Tkach, J.A., Taylor, M.D., 2021. Quantitative assessment of velocity and flow using compressed SENSE in children and young adults with adequate acquired temporal resolution. J. Cardiovasc. Magn. Reson. 23, 1–14. doi:10.1186/s12968-021-00811-7.

Krüger, G., Kastrup, A., Glover, G.H., 2001. Neuroimaging at 1.5 T and 3.0 T: Comparison of oxygenation-sensitive magnetic resonance imaging. Magn. Reson. Med. 45, 595–604. doi:10.1002/mrm.1081.

Labadie, C., Lee, J.H., Rooney, W.D., Jarchow, S., Aubert-Frécon, M., Springer Jr., C.S., Möller, H.E., 2014. Myelin water mapping by spatially regularized longitudinal relaxographic imaging at high magnetic fields. Magnetic Res. Med. 71, 375–387. doi:10.1002/mrm.24670.

Lescher, S., Jurcoane, A., Veit, A., Bähr, O., Deichmann, R., Hattingen, E., 2015. Quantitative T1 and T2 mapping in recurrent glioblastomas under bevacizumab: earlier detection of tumor progression compared to conventional MRI. Neuroradiology 57, 11–20. doi:10.1007/s00234-014-1445-9.

Leutritz, T., Seif, M., Helms, G., Samson, R.S., Curt, A., Freund, P., Weiskopf, N., 2020. Multiparameter mapping of relaxation (R1, R2*), proton density and magnetization transfer saturation at 3 T: A multicenter dual-vendor reproducibility and repeatability study. Hum. Brain Mapp. 41, 4232–4247. doi:10.1002/hbm.25122.

Lommers, E., Simon, J., Reuter, G., Delrue, G., Dive, D., Degueldre, C., Balteau, E., Phillips, C., Maquet, P., 2019. Multiparameter MRI quantification of microstructural tissue alterations in multiple sclerosis. Neuroimage Clin 23, 101879. doi:10.1016/j.nicl.2019.101879.

Lustig, M., Kim, S.-J., Pauly, J.M., 2008. A fast method for designing time-optimal gradient waveforms for arbitrary k-space trajectories. IEEE Trans. Med. Imaging 27, 866–873. doi:10.1109/TMI.2008.922699.

Mori, S., Wakana, S., Van Zijl, P.C., Nagae-Poetscher, L., 2005. MRI atlas of human white matter. Elsevier.

Murata, S., Hagiwara, A., Fujita, S., Haruyama, T., Kato, S., Andica, C., Kamagata, K., Goto, M., Hori, M., Yoneyama, M., 2021. Effect of hybrid of compressed sensing and parallel imaging on the quantitative values measured by 3D quantitative synthetic MRI: A phantom study. Magn. Reson. Imaging 78, 90–97. doi:10.1016/j.mri.2021.01.001.

Mussard, E., Hilbert, T., Forman, C., Meuli, R., Thiran, J.P., Kober, T., 2020. Accelerated MP2RAGE imaging using Cartesian phyllotaxis readout and compressed sensing reconstruction. Magn. Reson. Med. 84, 1881–1894. doi:10.1002/mrm.28244.

Nam, J.G., Lee, J.M., Lee, S.M., Kang, H.-J., Lee, E.S., Hur, B.Y., Yoon, J.H., Kim, E., Doneva, M., 2019. High acceleration three-dimensional T1-weighted dual echo Dixon hepatobiliary phase imaging using compressed sensing-sensitivity encoding: comparison of image quality and solid lesion detectability with the standard T1-weighted sequence. Korean J. Radiol. 20, 438. doi:10.3348/kjr.2018.0310.

NIST, 2020. Report of Measurement: Magnetic Resonance Measurements for MRI Biomarkers: Proton Spin Relaxation Times. National Institute of Standards and Technology, pp. 1–16 JUN 10, 2020.

Papp, D., Callaghan, M.F., Meyer, H., Buckley, C., Weiskopf, N., 2016. Correction of inter-scan motion artifacts in quantitative R1 mapping by accounting for receive coil sensitivity effects. Magn. Reson. Med. 76, 1478–1485. doi:10.1002/mrm.26058.

Peters, A.M., Brookes, M.J., Hoogenraad, F.G., Gowland, P.A., Francis, S.T., Morris, P.G., Bowtell, R., 2007. T2* measurements in human brain at 1.5, 3 and 7 T. Magn. Reson. Imaging 25, 748–753. doi:10.1016/j.mri.2007.02.014.

Poblador Rodriguez, E., Moser, P., Auno, S., Eckstein, K., Dymerska, B., van der Kouwe, A., Gruber, S., Trattnig, S., Bogner, W., 2021. Real-time motion and retrospective coil sensitivity correction for CEST using volumetric navigators (vNavs) at 7T. Magn. Reson. Med. 85, 1909–1923. doi:10.1002/mrm.28555.

Preibisch, C., Deichmann, R., 2009. Influence of RF spoiling on the stability and accuracy of T1 mapping based on spoiled FLASH with varying flip angles. Magn. Reson. Med. 61, 125–135. doi:10.1002/mrm.21776.

Pruessmann, K.P., Weiger, M., Scheidegger, M.B., Boesiger, P., 1999. SENSE: sensitivity encoding for fast MRI. Magn. Reson. Med. 42, 952–962. doi:10.1002/(SICI)1522-2594(199911)42:5<952::AID-MRM16>3.0.CO;2-S.

Reitz, S.C., Hof, S.-M., Fleischer, V., Brodski, A., Gröger, A., Gracien, R.-M., Droby, A., Steinmetz, H., Ziemann, U., Zipp, F., 2017. Multi-parametric quantitative MRI of normal appearing white matter in multiple sclerosis, and the effect of disease activity on T2. Brain Imaging. Behav. 11, 744–753. doi:10.1007/s11682-016-9550-5.

Sartoretti, T., Reischauer, C., Sartoretti, E., Binkert, C., Najafi, A., Sartoretti-Schefer, S., 2018. Common artefacts encountered on images acquired with combined compressed sensing and SENSE. Insights Imag. 9, 1107–1115. doi:10.1007/s13244-018-0668-4.

Seif, M., Curt, A., Thompson, A.J., Grabher, P., Weiskopf, N., Freund, P., 2018. Quantitative MRI of rostral spinal cord and brain regions is predictive of functional recovery in acute spinal cord injury. Neuroimage Clin. 20, 556–563. doi:10.1016/j.nicl.2018.08.026.

Seiler, A., Nöth, U., Hok, P., Reiländer, A., Maiworm, M., Baudrexel, S., Meuth, S., Rosenow, F., Steinmetz, H., Wagner, M., 2021. Multiparametric quantitative MRI in neurological diseases. Front. Neurol. 12, 287. doi:10.3389/fneur.2021.640239.

Smith, S.M., Jenkinson, M., Woolrich, M.W., Beckmann, C.F., Behrens, T.E., Johansen-Berg, H., Bannister, P.R., De Luca, M., Drobnjak, I., Flitney, D.E., 2004. Advances in functional and structural MR image analysis and implementation as FSL. Neuroimage 23, S208–S219. doi:10.1016/j.neuroimage.2004.07.051.

Stikov, N., Boudreau, M., Levesque, I.R., Tardif, C.L., Barral, J.K., Pike, G.B., 2015. On the accuracy of T1 mapping: searching for common ground. Magn. Reson. Med. 73, 514–522. doi:10.1002/mrm.25135.

Streitbürger, D.-P., Möller, H.E., Tittgemeyer, M., Hund-Georgiadis, M., Schroeter, M.L., Mueller, K., 2012. Investigating structural brain changes of dehydration using voxel-based morphometry. PLoS One 7, e44195. doi:10.1371/journal.pone.0044195.

Sullivan, D.C., Obuchowski, N.A., Kessler, L.G., Raunig, D.L., Gatsonis, C., Huang, E.P., Kondratovich, M., McShane, L.M., Reeves, A.P., Barboriak, D.P., 2015. Metrology standards for quantitative imaging biomarkers. Radiology 277, 813–825. doi:10.1148/radiol.2015142202.

Tabelow, K., Balteau, E., Ashburner, J., Callaghan, M.F., Draganski, B., Helms, G., Kherif, F., Leutritz, T., Lutti, A., Phillips, C., 2019. hMRI–A toolbox for quantitative MRI in neuroscience and clinical research. Neuroimage 194, 191–210. doi:10.1016/j.neuroimage.2019.01.029.

Taylor, B.N., Kuyatt, C.E., 1994. Guidelines for evaluating and expressing the uncertainty of NIST measurement results. doi:10.6028/NIST.tn.1297.

Teixeira, R.P.A., Malik, S.J., Hajnal, J.V., 2019. Fast quantitative MRI using controlled saturation magnetization transfer. Magn. Reson. Med. 81, 907–920. doi:10.1002/mrm.27442.

Tofts, P., 2003. Quantitative MRI of the Brain: Measuring Changes Caused by Disease. Wiley, Chichester, West Sussex; Hoboken, NJ, p. 633. doi:10.1002/0470869526 pp. xvi.

Vranic, J., Cross, N., Wang, Y., Hippe, D., De Weerdt, E., Mossa-Basha, M., 2019. Compressed sensing–sensitivity encoding (CS-SENSE) accelerated brain imaging: reduced scan time without reduced image quality. AJNR Am. J. Neuroradiol. 40, 92–98. doi:10.3174/ajnr.A5905.

Wansapura, J.P., Holland, S.K., Dunn, R.S., Ball Jr., W.S., 1999. NMR relaxation times in the human brain at 3.0 tesla. J. Mag. Res. Imaging 9, 531–538. doi:10.1002/(SICI)1522-2586(199904)9:4<531::AID-JMRI4>3.0.CO;2-L.

Wehrli, F., MacFall, J., Glover, G., Grigsby, N., Haughton, V., Johanson, J., 1984. The dependence of nuclear magnetic resonance (NMR) image contrast on intrinsic and pulse sequence timing parameters. Magn. Reson. Imaging 2, 3–16. doi:10.1016/0730-725x(84)90119-x.

Weiskopf, N., Callaghan, M.F., Josephs, O., Lutti, A., Mohammadi, S., 2014. Estimating the apparent transverse relaxation time (R2*) from images with different contrasts (ESTATICS) reduces motion artifacts. Front. Neurosci. 8, 278. doi:10.3389/fnins.2014.00278.

Weiskopf, N., Edwards, L.J., Helms, G., Mohammadi, S., Kirilina, E., 2021. Quantitative magnetic resonance imaging of brain anatomy and in vivo histology. Nature Reviews Physics 3, 1–19. doi:10.1038/s42254-021-00326-1.

Weiskopf, N., Mohammadi, S., Lutti, A., Callaghan, M.F., 2015. Advances in MRI-based computational neuroanatomy: from morphometry to in-vivo histology. Curr. Opin. Neurol. 28, 313–322. doi:10.1097/WCO.0000000000000222.

Weiskopf, N., Suckling, J., Williams, G., Correia, M.M., Inkster, B., Tait, R., Ooi, C., Bullmore, E.T., Lutti, A., 2013. Quantitative multi-parameter mapping of R1, PD*, MT, and R2* at 3T: a multi-center validation. Front. Neurosci. 7, 95. doi:10.3389/fnins.2013.00095.

Wright, P., Mougin, O., Totman, J., Peters, A., Brookes, M., Coxon, R., Morris, P., Clemence, M., Francis, S., Bowtell, R., 2008. Water proton T 1 measurements in brain tissue at 7, 3, and 1.5 T using IR-EPI, IR-TSE, and MPRAGE: results and optimization. MAGMA 21, 121–130. doi:10.1007/s10334-008-0104-8.

Yarach, U., Saekho, S., Setsompop, K., Suwannasak, A., Boonsuth, R., Wantanajittikul, K., Angkurawaranon, S., Angkurawaranon, C., Sangpin, P., 2021. Feasibility of accelerated 3D T1-weighted MRI using compressed-SENSE: Application to Quantitative Volume Measurement of Human Brain Structures. MAGMA doi:10.1007/s10334-021-00939-8.

Yarnykh, V.L., 2007. Actual flip-angle imaging in the pulsed steady state: a method for rapid three-dimensional mapping of the transmitted radiofrequency field. Magn. Reson. Med. 57, 192–200. doi:10.1002/mrm.21120.

Ziegler, G., Grabher, P., Thompson, A., Altmann, D., Hupp, M., Ashburner, J., Friston, K., Weiskopf, N., Curt, A., Freund, P., 2018. Progressive neurodegeneration following spinal cord injury: implications for clinical trials. Neurology 90, e1257–e1266. doi:10.1212/WNL.0000000000005258.

Appendix A

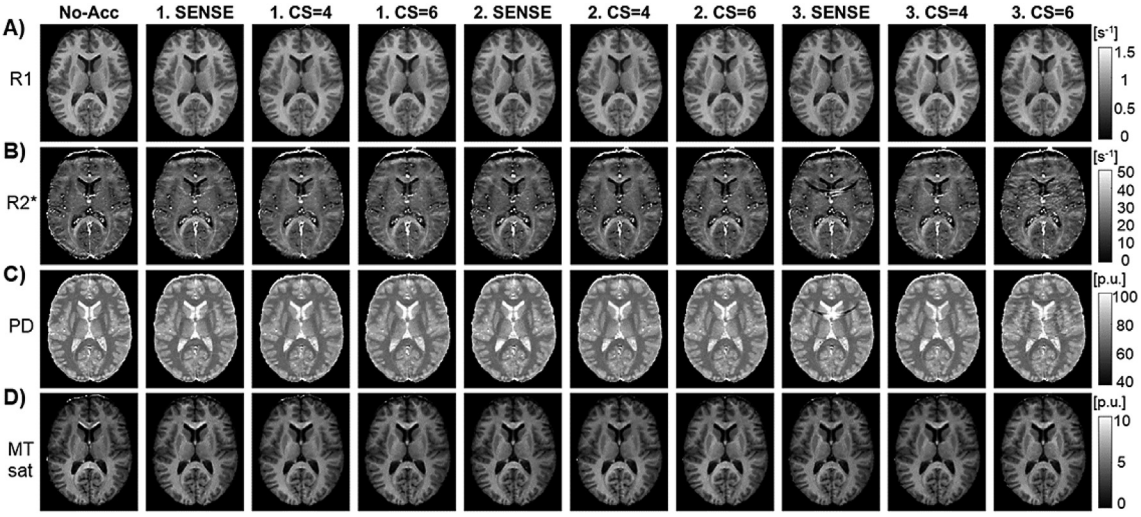

Supplementary Figure S1. Quantitative parameter maps of all accelerations and scan sessions of the participant where artifacts were encountered. R1 (A), R2* (B), PD (C), and MTsat (D) maps are shown for the non-accelerated sequence and the three repetitions of the sequences accelerated with SENSE = 2.5, CS = 4, and CS = 6 (columns). Artifacts can be seen in the R2* and PD maps of the third scan session for SENSE and CS=6.

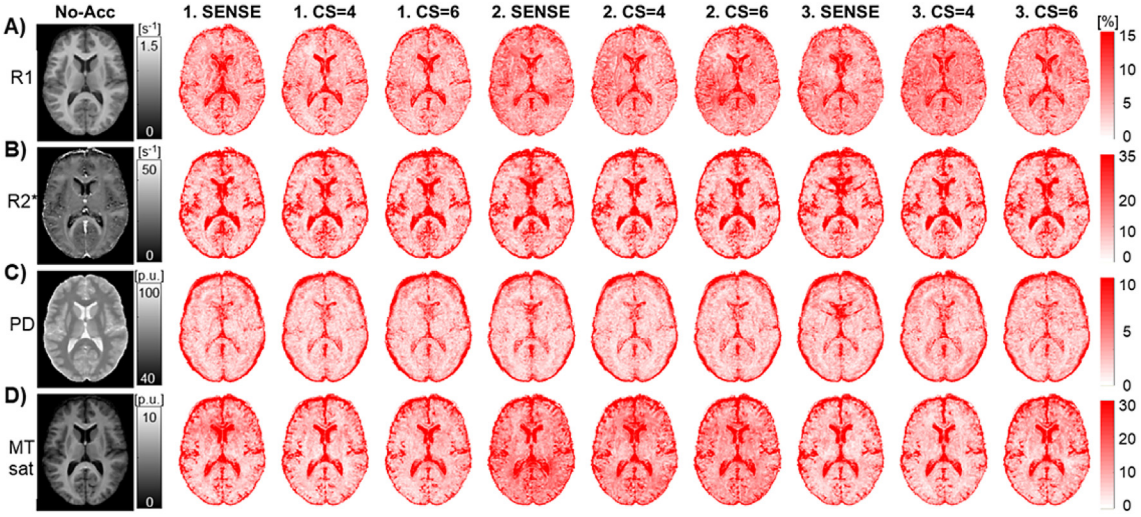

Supplementary Figure S2. Subject-average of non-accelerated parameter maps together with their subject-average absolute differences to quantitative parameter maps from all accelerated sequences and scan sessions. The subject-average of non-accelerated reference images of R1 (A), R2* (B), PD (C), and MTsat (D) are shown in the first column. Absolute difference maps were calculated between the non-accelerated reference images and the three repetitions of the sequences accelerated with SENSE = 2.5, CS = 4, and CS = 6 and averaged across all participants (second column to last column). Differences are given in percent deviations from the non-accelerated data. Color bars were adjusted for each parameter map.

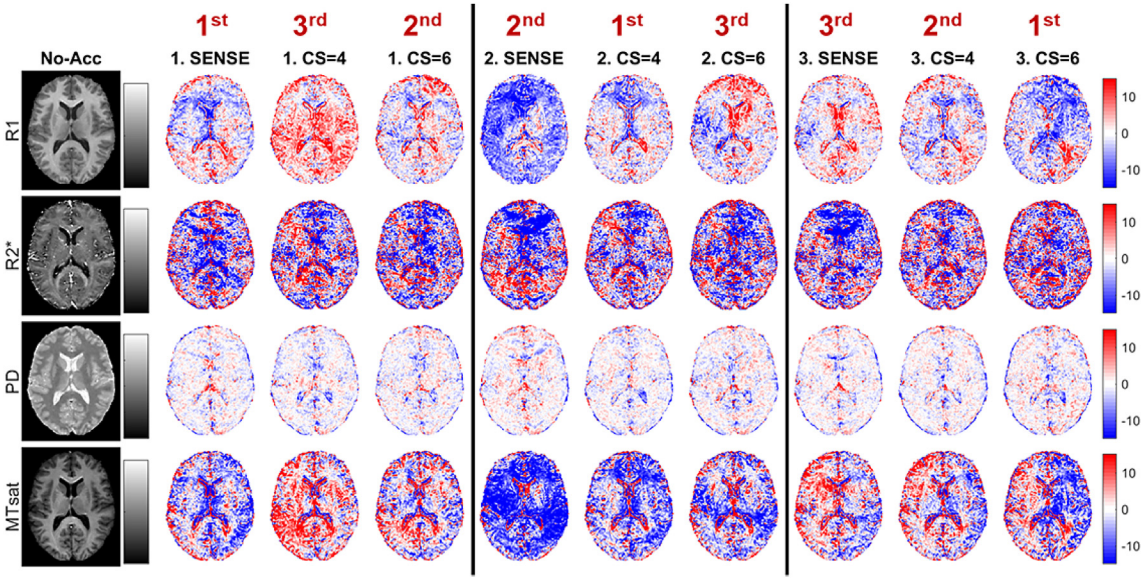

Supplementary Figure S3. Representative non-accelerated parameter maps of a single participant (left) together with their differences to quantitative parameter maps from all accelerated sequences and scan sessions. The non-accelerated reference images of R1 (A), R2* (B), PD (C), and MTsat (D) are shown in the first column (from the same volunteer as in Figure 2). Difference maps were calculated between the non-accelerated reference (left column) and the three repetitions of the sequences accelerated with SENSE = 2.5, CS = 4, and CS = 6 (second column to last column). Differences are given in percent deviations from the non-accelerated data. The acquisition order of accelerated data in each scan session is indicated in red in the top row.

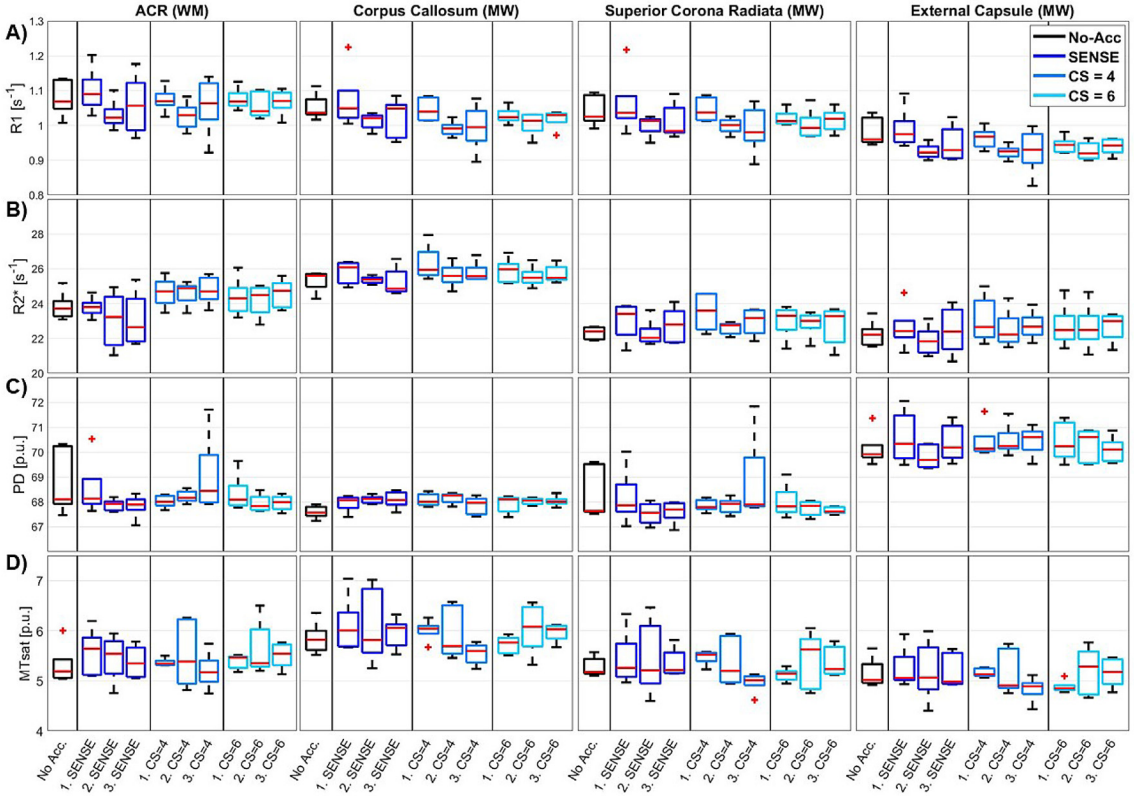

Supplementary Figure S4. Boxplots of average quantitative parameter values within several anatomical WM VOIs across subjects. The VOI-average values of R1 (A), R2* (B), PD (C), and MTsat (D) are shown for the anterior corona radiata (1st column) as in Figure 4 and three additional WM VOIs: the corpus callosum (2nd column), the superior corona radiata (3rd column), and the external capsule (last column). The VOI of the anterior corona radiata comprised ~13,100 voxels, corpus callosum ~25,900 voxels, the superior corona radiata ~14,500 voxels, and the external capsule ~3,700 voxels. The red line represents the median, the edges of the box indicate the 25th and 75th percentiles, the whiskers extend to the most extreme data points not considering outliers, and red +-symbols represent outliers.

Supplementary Table S5

Probability values from the repeated measures ANOVA testing for statistically significant differences between imaging accelerations in VOI-average quantitative parameter values. For each combination of parameters (R1, R2*, PD, and MTsat) and VOIs, a separate repeated measures ANOVA was performed. The assumption of sphericity was met for all data sets. Statistically significant p-values (< 0.05) are highlighted in bold font.

Within-subjects effects	Whole-brain GM	Thalamus	Whole-brain WM	ACR (WM)
R1	0.505	0.248	0.127	0.488
R2*	0.155	0.26	0.21	**0.019**
PD	0.053	**0.035**	calibrated	0.364
MTsat	0.946	0.458	0.819	0.596

Supplementary Table S6

Mean difference values from pairwise comparisons between all six pairs of acceleration methods for the combinations of parameters and VOIs that had a significant p-value in the repeated measures ANOVA. Paired two-tailed *t*-tests were performed for the ACR VOI of the R2* data and for the thalamus VOI of the PD data. No adjustment for multiple comparisons was performed. Statistically significant mean differences (with p-values < 0.05) are highlighted in bold font.

mean difference – *t*-test	No-Acc – SENSE	No-Acc – CS=4	No-Acc – CS=6	SENSE – CS=4	SENSE – CS=6	CS=4 – CS=6
R2* – ACR (WM) [s^{-1}]	0.516	-0.844	-0.544	**-1.360**	**-1.060**	0.300
PD – Thalamus (GM) [p.u.]	-0.214	**0.536**	0.170	**0.750**	0.384	-0.366

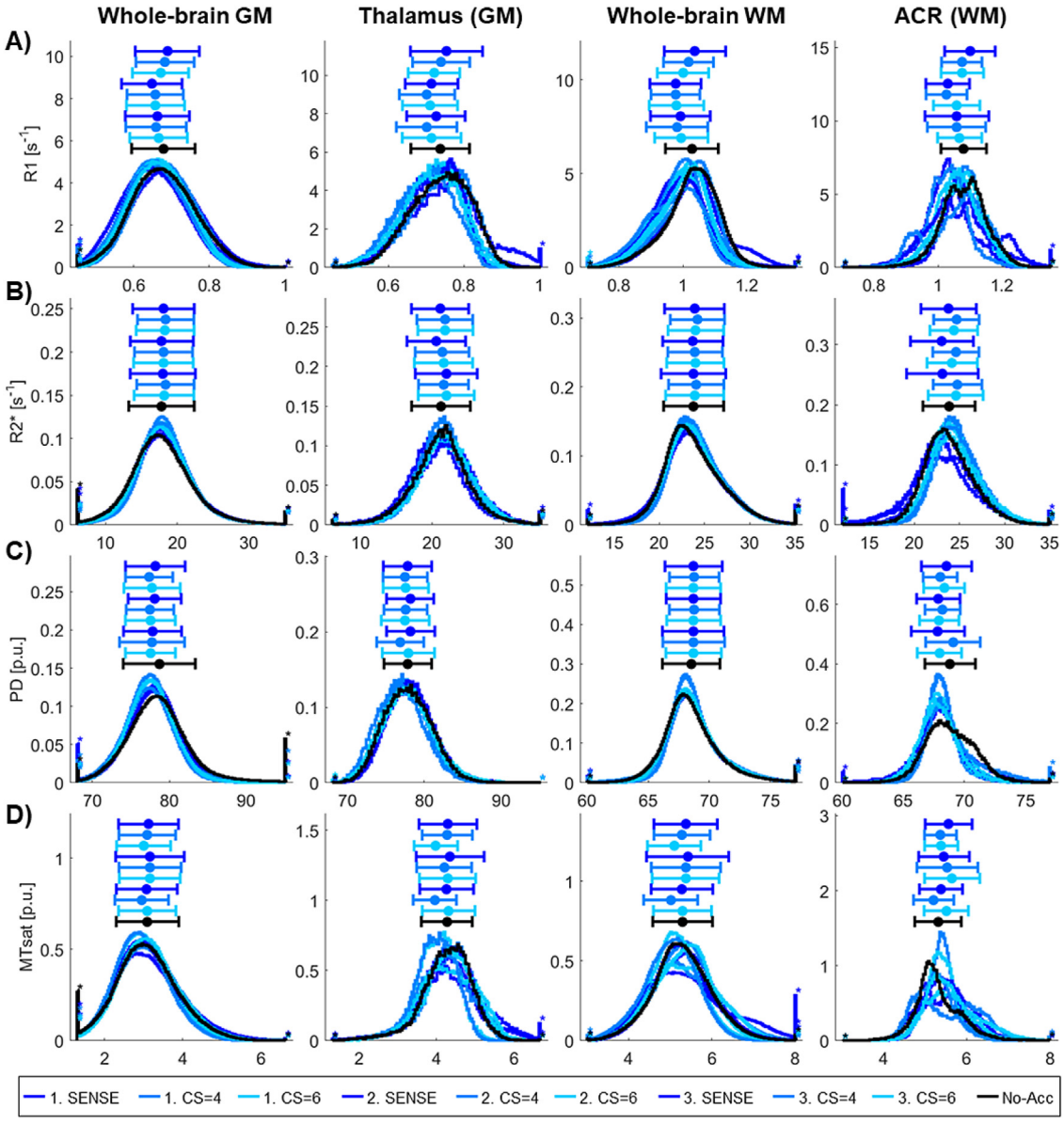

Supplementary Figure S7. Histograms of quantitative parameter values within GM and WM VOIs across subjects. Each histogram comprises the values from all voxels within whole-brain GM (1st column) and WM (3rd column) segmentations, within the thalamus (2nd column), and within the anterior corona radiata (4th column) of all five participants. Histograms are shown for R1 (A), R2* (B), PD (C), and MTsat (D) and for each of the 10 acquisitions either using various acceleration methods (different colors) or being acquired within different scan sessions. The mean and standard deviations of each histogram are provided as data points with error bars above the histogram lines. The legend below the graphs lists from top to bottom the scan session as well as acceleration technique and factor for the plots of mean and standard deviation values above each histogram. These graphs were created based on (Lansey, 2021).

Reference: Lansey, J.C., 2021. Plot and compare histograms; pretty by default. MATLAB Central File Exchange.

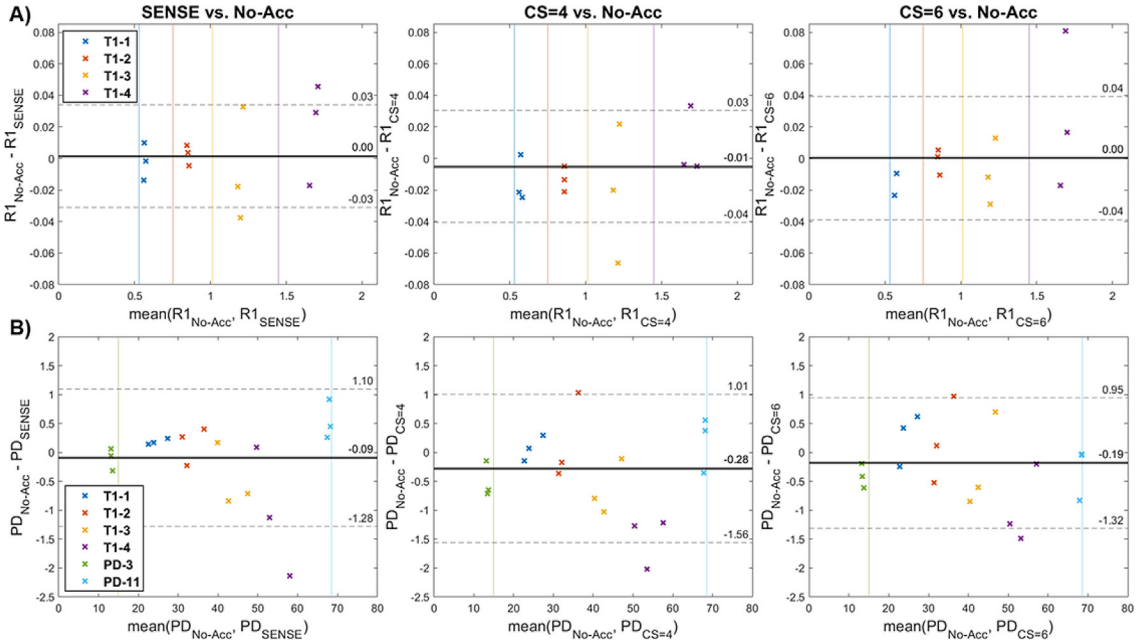

Supplementary Figure S8. Bland-Altman plots comparing VOI-average quantitative parameter values between non-accelerated and accelerated data using either SENSE = 2.5, CS = 4, or CS = 6 (columns) of the phantom data. The four VOI-average parameter values of R1 in s^{-1} (A) and the six VOI-average parameter values of PD in p.u. (B) from the three repeated accelerated measurements were compared with the three repeated measurements of the non-accelerated parameter values. Additionally, average difference values are shown as black lines, 95% limits of agreement (average difference ±1.96 standard deviations of differences) as dashed lines, and the literature reference values of R1 and PD as colored vertical lines.

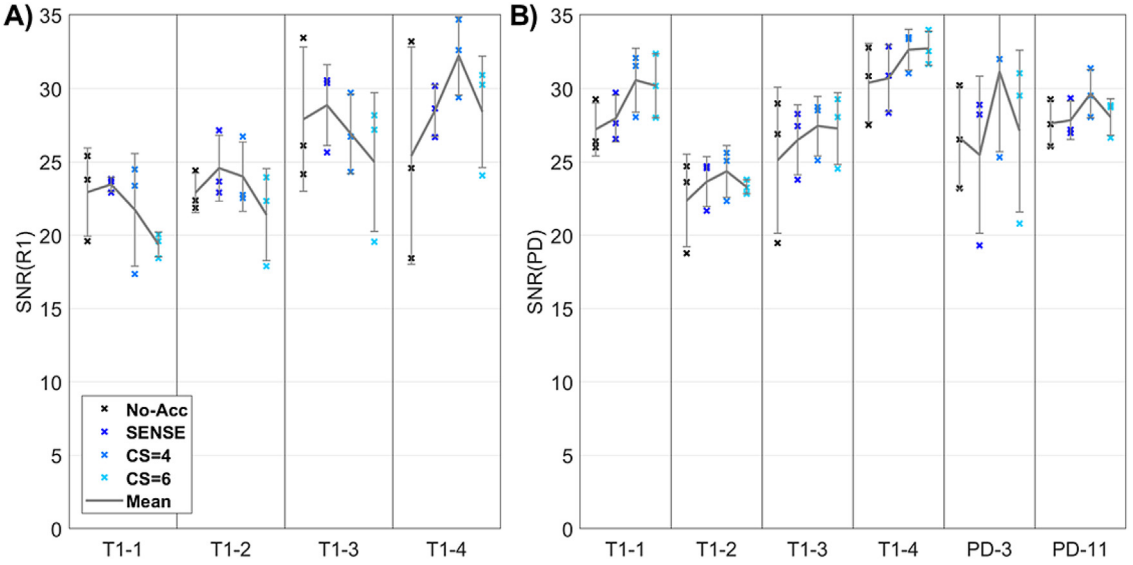

Supplementary Figure S9. VOI-average signal-to-noise ratios (SNR) of R1 (A) and PD (B) within phantom reference regions. The SNR values are shown for the selected volume-of-interest values (columns) from data acquired using different imaging accelerations (colors). The mean across the three repetitions acquired with the same imaging acceleration is indicated by a gray line. Error bars indicate the standard deviations across the three repetitions.

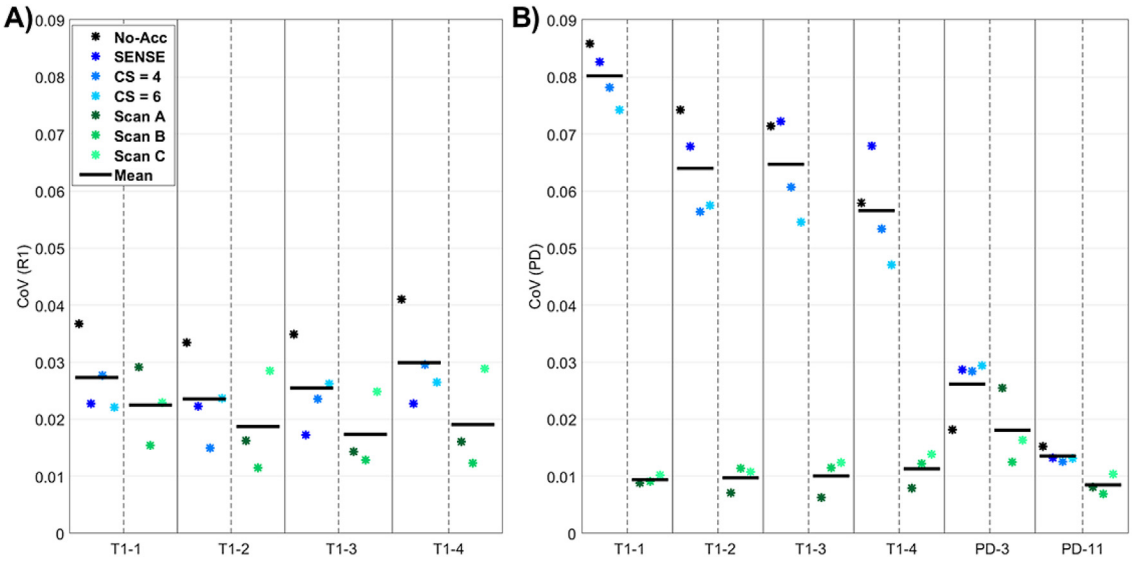

Supplementary Figure S10. Coefficients of variation (CoV) of the quantitative parameter maps from the repeatability (blue) and reproducibility (green) measurements of the phantom data. In each panel, the VOI-average CoV values of R1 (A) and PD (B) are shown for the selected VOIs. The CoV values for Scan A, Scan B, and Scan C were calculated based on the accelerated data sets (SENSE = 2.5, CS = 4, and CS = 6) but without the non-accelerated data. The mean of the four ("repeatability") or three ("reproducibility") values per factor is represented with a black line for each parameter and volume-of-interest.